

The Observed Water Vapor Budget in an Atmospheric River over the Northeast Pacific

JOEL R. NORRIS,^a F. MARTIN RALPH,^a REUBEN DEMIRDJIAN,^a FOREST CANNON,^a BYRON BLOMQUIST,^{b,c}
CHRISTOPHER W. FAIRALL,^c J. RYAN SPACKMAN,^d SIMONE TANELLI,^e AND DUANE E. WALISER^e

^a Center for Western Weather and Water Extremes, Scripps Institution of Oceanography, University of California, San Diego, La Jolla, California; ^b Cooperative Institute for Research in the Environmental Sciences, Boulder, Colorado; ^c NOAA/Earth System Research Laboratory/Physical Sciences Division, Boulder, Colorado; ^d Science and Technology Corporation, NOAA/Earth System Research Laboratory, Boulder, Colorado; ^e Jet Propulsion Laboratory, California Institute of Technology, Pasadena, California

(Manuscript received 26 February 2020, in final form 1 July 2020)

ABSTRACT: Combined airborne, shipboard, and satellite measurements provide the first observational assessment of all major terms of the vertically integrated water vapor (IWV) budget for a 150 km × 160 km region within the core of a strong atmospheric river over the northeastern Pacific Ocean centered on 1930 UTC 5 February 2015. Column-integrated moisture flux convergence is estimated from eight dropsonde profiles, and surface rain rate is estimated from tail Doppler radar reflectivity measurements. Dynamical convergence of water vapor ($2.20 \pm 0.12 \text{ mm h}^{-1}$) nearly balances estimated precipitation ($2.47 \pm 0.41 \text{ mm h}^{-1}$), but surface evaporation ($0.0 \pm 0.05 \text{ mm h}^{-1}$) is negligible. Advection of drier air into the budget region ($-1.50 \pm 0.21 \text{ mm h}^{-1}$) causes IWV tendency from the sum of all terms to be negative ($-1.66 \pm 0.45 \text{ mm h}^{-1}$). An independent estimate of IWV tendency obtained from the difference between IWV measured by dropsonde and retrieved by satellite 3 h earlier is less negative ($-0.52 \pm 0.24 \text{ mm h}^{-1}$), suggesting the presence of substantial temporal variability that is smoothed out when averaging over several hours. The calculation of budget terms for various combinations of dropsonde subsets indicates the presence of substantial spatial variability at ~50-km scales for precipitation, moisture flux convergence, and IWV tendency that is smoothed out when averaging over the full budget region. Across subregions, surface rain rate is linearly proportional to dynamical convergence of water vapor. These observational results improve our understanding of the thermodynamic and kinematic processes that control IWV in atmospheric rivers and the scales at which they occur.


KEYWORDS: Precipitation; Conservation equations; Moisture/moisture budget; Dropsondes; Radars/Radar observations; Satellite observations


1. Introduction

Atmospheric rivers (ARs) are longitudinally narrow regions of the atmosphere that have large integrated water vapor (IWV) and integrated water vapor transport (IVT), accounting for over 90% of the poleward flux of water vapor across middle latitudes (Zhu and Newell 1998; Guan and Waliser 2015). They typically occur ahead of cold fronts in the warm, moist sector of an extratropical cyclone, and the direction of water vapor transport is oriented approximately parallel to the cold front (Ralph et al. 2004; American Meteorological Society 2019). Water vapor transport is greatest 1–2 km above the surface because of large humidity in the near-saturated lower troposphere and the frequent occurrence of a low-level jet (Ralph et al. 2017). Substantial precipitation and flooding in many regions around the world can sometimes result when ARs encounter land (Lavers and Villarini 2013; Paltan et al. 2017;

Viale et al. 2018), especially as the water vapor transport is forced upslope due to coastal orography (Ralph et al. 2006; Neiman et al. 2011). The importance of ARs to water supply and flood danger has motivated observational campaigns to understand the processes that increase and decrease IWV.

Previous observational campaigns (e.g., Neiman et al. 2014, 2016) investigated ARs over the northeastern Pacific Ocean using in situ aircraft observations and dropsondes. While satellites can report the spatial distribution of IWV, only in situ measurements can obtain the vertical profile of water vapor and winds in the lower troposphere that are necessary for calculating IVT (e.g., Ralph et al. 2017). Airborne deployment of dropsondes around the perimeter of a region allows the convergence or divergence of water vapor into that region to be calculated (Neiman et al. 2014). Convergence of water vapor will increase IWV within the region (Bao et al. 2006), and divergence of water vapor will decrease IWV. Also, evaporation from the surface will increase IWV, and precipitation reaching the surface will decrease IWV (Cordeira et al. 2013). These mechanisms were confirmed by the recent study of Guan et al. (2020), who employed reanalysis data to document how convergence, divergence, and advection of water vapor together with precipitation and evaporation contributed to the time tendency in IWV in different sectors of atmospheric rivers. In particular, Guan et al. found that the largest differences between reanalyses occurred in the core of ARs, where IVT was greatest. Here, the IWV tendency was driven

 Denotes content that is immediately available upon publication as open access.

 Supplemental information related to this paper is available at the Journals Online website: <https://doi.org/10.1175/JHM-D-20-0048.s1>.

Corresponding author: Joel Norris, jnorris@ucsd.edu

DOI: 10.1175/JHM-D-20-0048.1

© 2020 American Meteorological Society. For information regarding reuse of this content and general copyright information, consult the AMS Copyright Policy (www.ametsoc.org/PUBSReuseLicenses).

by the difference between large opposing contributions from precipitation and the dynamical convergence of water vapor. This was also the sector of an AR with the greatest uncertainty in IWV tendency because of disagreements between reanalyses over the magnitude of dynamical convergence of water vapor and the partitioning between convective and stratiform precipitation. The disagreements between reanalyses and the inability of reanalyses to obtain budget closure underscore the need to observationally quantify the magnitudes of dynamical convergence and precipitation and their contributions to IWV tendency in the AR core.

It has been challenging to obtain quantitative precipitation estimates in ARs over the ocean ahead of landfall due to the lack of observations, thus motivating the CalWater field studies (Ralph et al. 2016). The present study employs CalWater2 observations on 5 February 2015 from the NOAA G-IV and the NOAA Research Vessel (R/V) *Ronald H. Brown* (RHB) to derive a spatial estimate of precipitation over an $\sim 24\,000\text{-km}^2$ oceanic domain off the California coast during an AR event. As an advance beyond Neiman et al. (2016, 2017), measurements of radar reflectivity Z are converted to rain rate R using a Z - R relationship derived from a shipboard disdrometer. This, together with observations of evaporation and convergence of IVT, enables all major terms in the integrated water vapor budget to be quantified. The subtraction of precipitation from the sum of IVT convergence and evaporation furthermore yields an estimate of the time tendency of IWV within the budget region. This can be compared with an independent observational assessment of the IWV time tendency, from which the water vapor budget of the AR region can be observationally closed. An essential requirement for determining closure is calculation of robust estimates of uncertainty for every term of the budget, something lacking in previous studies (e.g., Neiman et al. 2014).

Additional physical insight into processes controlling AR IWV is gained by calculating water vapor budget terms for subregions within the larger budget region. The resulting values show how much spatial variability in IWV convergence and precipitation is present at scales of 50–100 km, something not investigated by previous studies. Separation of IVT convergence into a component representing the IWV tendency due to horizontal advection and a component representing the IWV tendency due to dynamical convergence (Seager and Henderson 2013; Wong et al. 2016) is useful for investigating the relationship between dynamical convergence and precipitation. Moreover, the impact of advection can be mitigated in the water vapor budget by examining IWV tendency in the Lagrangian rather than Eulerian frame of reference. The detailed observational characterization by the present study of the magnitude and uncertainty of different terms of the water vapor budget and the scales at which they will occur will improve our understanding of physical processes driving changes in IWV within the core of an AR and inform planning for future observational campaigns.

2. Observing systems and gridded datasets

As described in Neiman et al. (2016, 2017), airborne data were principally provided by the NOAA G-IV research

aircraft (<http://www.oma.noaa.gov/learn/aircraft-operations/aircraft/gulfstream-iv-sp-g-iv>). This aircraft flew at a cruising altitude of about 13.5 km and a speed of about 230 m s^{-1} , covering the water vapor budget region in approximately 50 min (Fig. 1). The G-IV deployed 34 dropsondes between 1836 and 2340 UTC 5 February 2015 at locations indicated in Fig. 1. Nine dropsondes were deployed in the water vapor budget region between 1910 and 1956 UTC, one of which failed to produce usable data (dropsonde 7 at 1927 UTC). The dropsondes reported horizontal wind velocity, pressure, temperature, and relative humidity as a function of height via the Airborne Vertical Atmospheric Profiling System (https://www.eol.ucar.edu/observing_facilities/avaps-dropsonde-system). Specific humidity was subsequently calculated from the latter parameters. The 0.5-s^{-1} dropsonde measurement rate corresponds to about 6-m vertical resolution near the surface, where specific humidity values are greatest. The tail Doppler radar (TDR) on the G-IV operated at an X-band frequency of 9.3 GHz (3.2-cm wavelength) and scanned 20° fore and aft of the fuselage's long axis with a beamwidth of 2.7° and an along-track resolution of 1125 m (based on flight speed and 7-s sweep time).

A secondary source of airborne data was the NOAA P-3 aircraft, which flew through the budget region at an elevation of about 2400 m (Fig. 1). The small-scale variations in wind velocity, temperature, and relative humidity measured by the NOAA P-3 along its flight track provide an estimate of the spatial standard deviation of these meteorological properties in the lower troposphere where water vapor transport is largest.

As described in Neiman et al. (2017), surface data were provided by the RHB (<https://oceanexplorer.noaa.gov/technology/vessels/ronbrown/ronbrown.html>), which was positioned at about 37°N , 127.2°W during the event on 5 February 2015. The RHB was equipped with a large array of instrumentation, including a Parsivel laser disdrometer that provided near-surface measurements of reflectivity and rain rate every 60 s (Löffler-Mang and Joss 2000). In situ measurements of pressure, temperature, relative humidity, and wind provided the data from which surface fluxes of latent and sensible heat were calculated. The coordinated G-IV overpass of the RHB occurred at 1950 UTC.

The Special Sensor Microwave Imager/Sounder (SSMIS) instrument on the *F16*, *F17*, and *F18* polar-orbiting satellites provided retrievals of IWV and rain rate (Hilburn and Wentz 2008; Kunkee et al. 2008; Wentz 1995). These data have a native resolution of about 40 km within swaths about 1700 km wide and had been mapped to a regular 0.25° grid by Remote Sensing Systems (www.remss.com/missions/ssmi/). The *F18* overpass at 1615 UTC 5 February 2015 was the closest satellite overpass in space and time to the NOAA G-IV aircraft flight through the budget region between 1910 and 1956 UTC on the same day. Morphed Integrated Microwave Imagery obtained from the Cooperative Institute for Meteorological Satellite Studies (CIMSS) at the University of Wisconsin–Madison (<http://tropic.ssec.wisc.edu/real-time/mimic-tpw/global/main.html>) provided IWV values on a regular hourly grid. This product had been constructed by advecting satellite-retrieved IWV by lower-tropospheric mean layer wind obtained from the

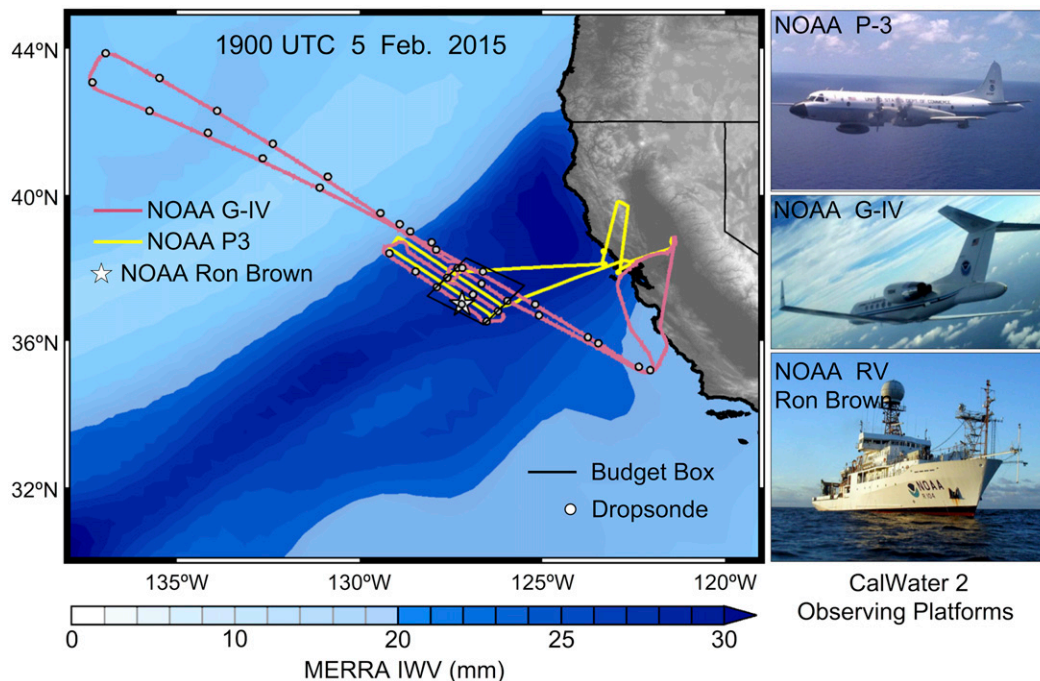


FIG. 1. (left) Flight tracks of NOAA G-IV (pink) and NOAA P-3 (yellow), locations of NOAA *RHB* (star) and dropsondes (circles), and boundary of water vapor budget region (black-outlined polygon), all overlaying MERRA-2 IWV for 1900 UTC 5 Feb 2015 (mm; color scale at bottom). (right) Photographs of the observing systems.

Global Forecast System to fill time and space gaps between satellite swaths (Wimmers and Velden 2011). Morphed Integrated Microwave Imagery was used only to characterize the synoptic overview and not for water budget calculations.

The Modern-Era Retrospective Analysis for Research and Applications, version 2 (MERRA-2) (Gelaro et al. 2017), provided information on the large-scale synoptic environment in which the atmospheric river occurred. The MERRA-2 reanalysis winds, temperature, humidity, and sea level pressure were available every 3 h on a $0.5^\circ \times 0.625^\circ$ latitude–longitude grid at intervals of 25 hPa from 1000 to 700 hPa and intervals of 50 hPa from 700 to 100 hPa.

3. Synoptic overview

On 1800 UTC 4 February 2015, a strong cyclonically curved AR was located approximately 500 km from the U.S. West Coast on the southeastern side of a surface cyclone (Figs. 2a and 3a). The IVT values in the AR exceeded $1050 \text{ kg m}^{-1} \text{ s}^{-1}$, denoting it as “extreme” according to the AR intensity scale of Ralph et al. (2019). A cold front occurred northwest of the AR, as indicated by the gradient in 925-hPa equivalent potential temperature θ_e , and upward vertical motion existed within the AR (Fig. 4a). The surface cyclone center appeared in the left exit region of a strong zonally oriented 300-hPa jet streak where the secondary transverse circulation favored quasigeostrophic ascent and further cyclone deepening (Fig. 5a; Winters and Martin 2017).

Over the ensuing 24-h period, the surface cyclone deepened by approximately 6 hPa and tracked northeastward. The AR

region made landfall along the Oregon coast at 00 UTC 5 February 2015 and subsequently propagated southward along the coast, with the leading edge of the AR reaching the San Francisco Bay region around 1800 UTC 5 February (Figs. 2b and 3b). Peak IVT values strengthened slightly to $1070 \text{ kg m}^{-1} \text{ s}^{-1}$ and exhibited broader width, in part due to the weakened cold front and horizontal wind shear (Fig. 4b). The left exit region of the 300-hPa jet streak transitioned to south of the surface cyclone, an unfavorable position for further deepening (Fig. 5b). The aircraft measurements occurred shortly after 1800 UTC 5 February 2015, and the water budget region displayed in Figs. 2b, 3b, 4b, and 5b occurred in an area of large IWV, large IVT, and upward vertical velocity. This area was ahead of the cold front and in the “frontal” sector of the AR, according to the classification scheme of Guan et al. (2020).

By 1800 UTC 6 February 2015, the AR had become a straight line of IVT centered on the San Francisco Bay region (Figs. 2c and 3c). Maximum IVT remained strong, albeit decreasing slightly to $965 \text{ kg m}^{-1} \text{ s}^{-1}$. Notably, areas in coastal Northern California received more than 250 mm of precipitation over the 48-h period following landfall, according to the California Nevada River Forecast Center (not shown; <https://www.cnrfc.noaa.gov>). The associated surface cyclone weakened and moved farther northeastward as the AR propagated southeastward, thus disconnecting the two features. Over the next 24 h, the AR decayed substantially and moved southward along the California coast (Fig. 2d). Maximum IVT decreased to $575 \text{ kg m}^{-1} \text{ s}^{-1}$, and the AR became independent from the surface cyclone (Fig. 3d).

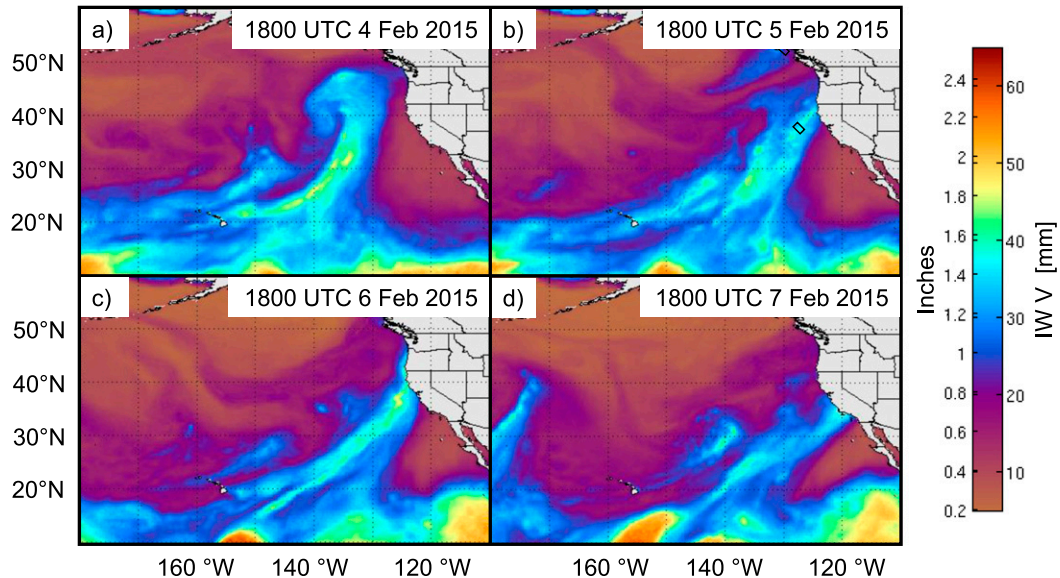


FIG. 2. Morphed Integrated Microwave Imagery of IWV (mm; color scale at right) for 1800 UTC (a) 4, (b) 5, (c) 6, and (d) 7 Feb 2015. The approximate location of the water vapor budget region is shown in a black-outlined polygon in (b). This figure is provided through the courtesy of CIMSS at the University of Wisconsin–Madison.

4. The NOAA G-IV airborne perspective

The NOAA G-IV observed the offshore AR environment during a single flight occurring during 1830–2340 UTC 5 February 2015 (Fig. 1). The aircraft flew several short and long legs perpendicular to the orientation of the AR while deploying a total of 34 dropsondes, 32 of which returned usable data (Table 1). Three legs across the axis of the AR were about 40–80 km apart in the AR-parallel direction. In this case, dropsondes from two or three different legs were averaged together if they were the same distance from the AR axis in order to provide a more robust and smoother representation of the cross-AR atmospheric structure. Figure 6 displays a southeast-to-northwest cross section approximately perpendicular to the AR axis that was constructed from 14 individual and averaged profiles from dropsondes deployed during the outbound portion of the G-IV flight as listed in Table 2. No time-to-space adjustment was applied.

A maximum IVT value of $1003 \text{ kg m}^{-1} \text{ s}^{-1}$ and a maximum IWV value of about 35 mm occurs in Fig. 6c, in general agreement with the satellite and reanalysis products displayed in Figs. 2b and 3b. The water vapor budget region, denoted by black vertical lines, contains the zone of greatest IWV and most of the zone of greatest IVT. Maximum specific humidity (10.6 g kg^{-1}), maximum water vapor flux ($3.2 \text{ kg m}^{-1} \text{ s}^{-1} \text{ hPa}^{-1}$), and a low-level jet (32.5 m s^{-1}) also occur within the budget region (Figs. 6a,b). Relatively strong winds in the lower troposphere and relatively weak winds in the upper troposphere result in nearly uniform wind speed with height inside the budget region. Slight directional wind shear is present with southerly winds near the surface veering to southwesterly winds near the tropopause, but the general barotropic structure is consistent with the budget region occurring distinctly ahead of the cold front (Fig. 6b). Most of the budget region below the 700-hPa level is close to saturation, as

demonstrated by the widespread area of relative humidity exceeding 90% (Fig. 6a).

Figure 7 displays a close-up view of the NOAA G-IV flight track marked with the release times for dropsondes comprising the $\sim 150 \text{ km} \times 160 \text{ km}$ region for which the water vapor budget is calculated. Following previous work and assuming steady translation velocity of the AR system over the measurement period (Neiman et al. 2014, 2016), the flight track and dropsonde locations were time-to-space adjusted to a common reference time of 1930 UTC (details provided in section 5f). This caused the originally parallel flight legs to become skewed as the atmospheric columns sampled by earlier dropsondes will have moved farther northeast by 1930 UTC and the atmospheric columns sampled by later dropsondes will have been farther southwest at 1930 UTC (Fig. S1 in the online supplemental material shows flight track and dropsonde locations without adjustment). Figure 8 displays surface rain rate derived from aircraft radar reflectivity measurements, also after application of time-to-space adjustment (Fig. S2 in the online supplemental material shows radar reflectivity and dropsonde surface locations without adjustment). The flight tracks overlie SSMIS satellite imagery of IWV (Fig. 7a) and rain rate (Fig. 7b) obtained from an earlier overpass of *F18* occurring at 1615 UTC to which time-to-space adjustment was applied (Fig. S1 in the online supplemental material shows satellite imagery without adjustment). The specific satellite imagery displayed in Fig. 7 was chosen according to the area within the entire satellite swath that exhibited a pattern of rain rate with the highest spatial correlation to the pattern of aircraft radar precipitation displayed in Fig. 8 (details provided in section 5f). Thus, the comma-shaped satellite rain rate pattern in Fig. 7b resembles the comma-shaped aircraft radar precipitation

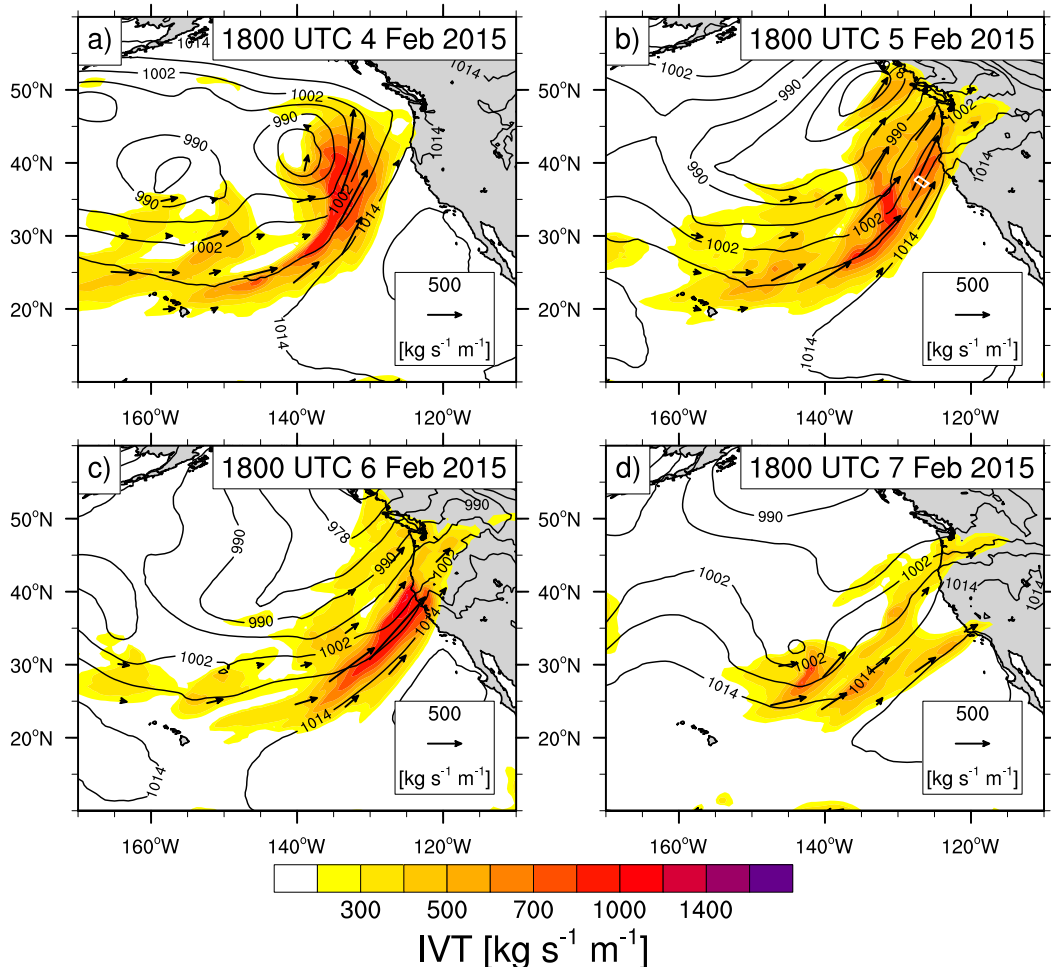


FIG. 3. Plan-view analyses of the 1000–100 hPa IVT ($\text{kg m}^{-1} \text{s}^{-1}$; magnitude color scale at bottom and vector scale at bottom right) and SLP (6-hPa interval; black contours) from the MERRA-2 dataset at 1800 UTC (a) 4, (b) 5, (c) 6, and (d) 7 Feb 2015. Every tenth IVT vector is plotted in longitude and latitude (6.25° spacing), but only if IVT exceeds $250 \text{ kg m}^{-1} \text{s}^{-1}$. The approximate location of the water vapor budget region is shown in a white-outlined polygon in (b).

pattern in Fig. 8 by construction and assumes temporal continuity of the overall precipitation cluster between the satellite overpass and the G-IV flight. If this assumption is invalid, then a different (and unknown) pattern of satellite IWV and rain rate will underlie the flight track in Fig. 7.

Figure 7a suggests that these three G-IV flight legs sampled an especially moist region within the larger AR. Although the highest satellite IWV values reach 40 mm , this may underestimate the local maximum since the occurrence of precipitation interferes with the retrieval of IWV. The dropsonde measurements in Table 1 agree with the satellite retrievals that IWV generally exceeds 30 mm in the water vapor budget region, but the fact that the dropsonde values from 1910 to 1956 UTC are generally smaller than the satellite values from 1615 UTC suggests that the amount of water vapor in a column moving with the AR may have declined over time. Figure 8 displays dropsonde winds measured at 925 hPa, which is near the level of average maximum moisture flux occurring at 940 hPa; the winds are

south-southwesterly at 30 ms^{-1} and exhibit little horizontal shear. The G-IV TDR indicates that precipitation is occurring over about half of the budget region, and radar-derived rain rates exceed 10 mm h^{-1} at many locations (Fig. 8). We also do not expect quantitative agreement between satellite-derived and radar-derived rain rate due to uncertainties in retrieval, differences in spatial resolution, and the 3-h difference between observation times.

Figure 9 displays vertical profiles of atmospheric properties calculated from the dropsondes in the water vapor budget region, both for individual dropsondes and the average across all eight dropsondes. The pressure level of dropsonde release (about 200 hPa) was considerably higher than the pressure level of the tropopause (about 300 hPa). Average wind speed is approximately uniform in the 400–950-hPa layer, and wind direction changes by less than 20° between the top and bottom of that layer. The occurrence of vertically uniform equivalent potential temperature in

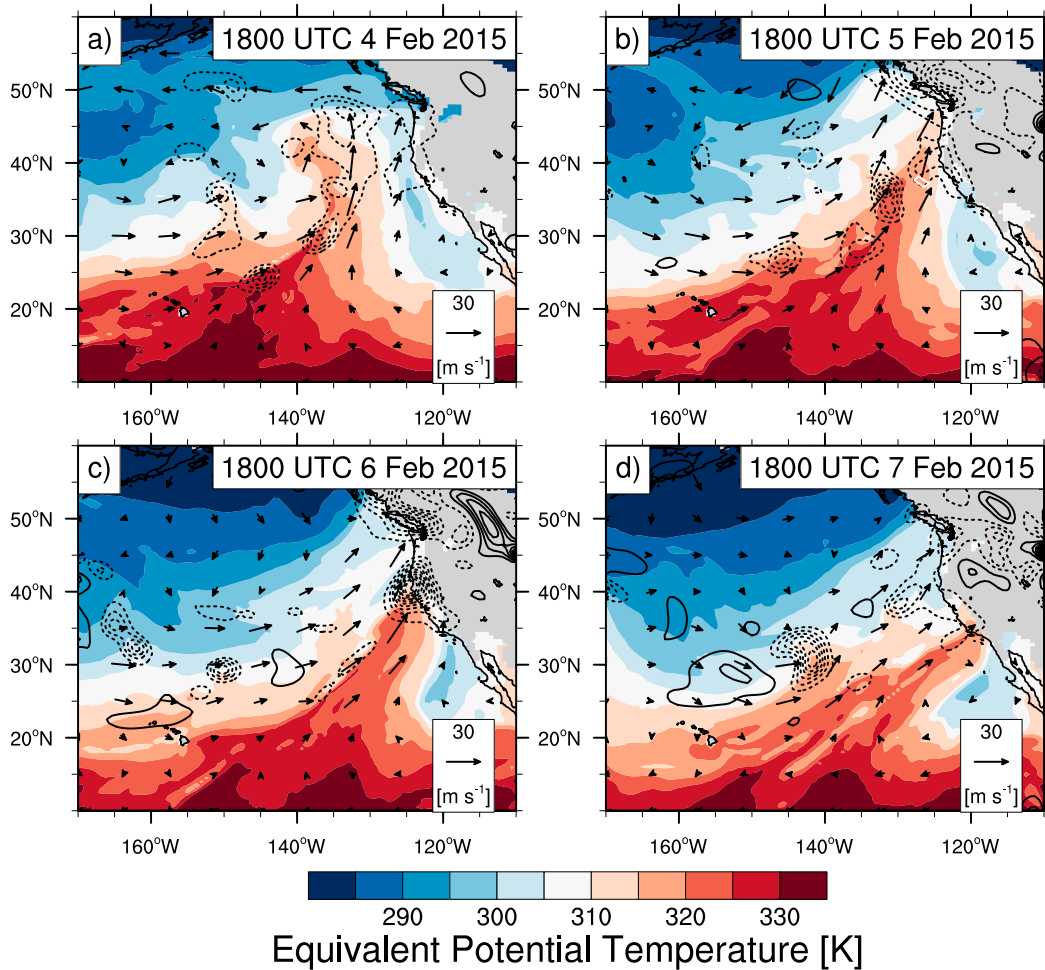


FIG. 4. As in Fig. 3, but from the MERRA-2 dataset for 925-hPa θ_e (K; color scale on bottom), 925-hPa wind velocity (vector scale at bottom right), and 700-hPa ω (plotted every 0.2 Pa s^{-1} , with solid black contours for positive, dashed black contours for negative, and no zero line). A 3×3 smoother was applied to wind and ω six times before plotting.

the 750–950-hPa layer suggests that saturated parcels will experience neutral stratification and have no resistance to lifting, as might occur when the low-level flow encounters coastal orography (Ralph et al. 2005). Average relative humidity was 85–95% in the lower troposphere with no dropsonde reporting relative humidity less than 70% and some dropsondes reporting layers with 100% relative humidity. The average profile appears to be somewhat drier at 900 hPa than above and below that level. Average moisture flux peaks at 940 hPa with a value of $3.0 \text{ kg m}^{-1} \text{ s}^{-1} \text{ hPa}^{-1}$ and consistently exceeds $2.0 \text{ kg m}^{-1} \text{ s}^{-1} \text{ hPa}^{-1}$ below the 800-hPa level. Several dropsondes have maximum values of $3.5 \text{ kg m}^{-1} \text{ s}^{-1} \text{ hPa}^{-1}$.

5. Water budget method

a. General approach

Following Seager and Henderson (2013), the water vapor budget for an atmospheric column at a fixed location may be represented in pressure coordinates as

$$\left. \frac{\partial \text{IWV}}{\partial t} \right|_{\text{Eul}} = \frac{1}{g\rho_w} \int_{p_{\text{top}}}^{p_0} -\nabla \cdot (q\mathbf{V}) dp - \frac{1}{g\rho_w} q_0 \mathbf{V}_0 \cdot \nabla p_0 + E - P, \quad (1)$$

where g is gravitational acceleration, ρ_w is the density of liquid water, q is specific humidity, \mathbf{V} is horizontal wind, E is evaporation from the surface, P is precipitation reaching the surface, and p_{top} and p_0 are the pressures at the top and bottom of the atmospheric column, respectively. Here, the subscript Eul is used as a reminder that the above IWV tendency is calculated in the Eulerian reference frame. Note that the first rhs term is the column-integrated moisture flux convergence (hereinafter called CIMC), and the second rhs term is moisture flux through a tilted bottom pressure surface (hereinafter called SFC) where q_0 and \mathbf{V}_0 are specific humidity and horizontal wind, respectively, on the bottom pressure surface. Cloud condensate is neglected because vertically integrated cloud condensate is two orders of magnitude smaller than IWV.

The CIMC may be separated into a first term that is the column integral of horizontal advection of water vapor (ADV) and a

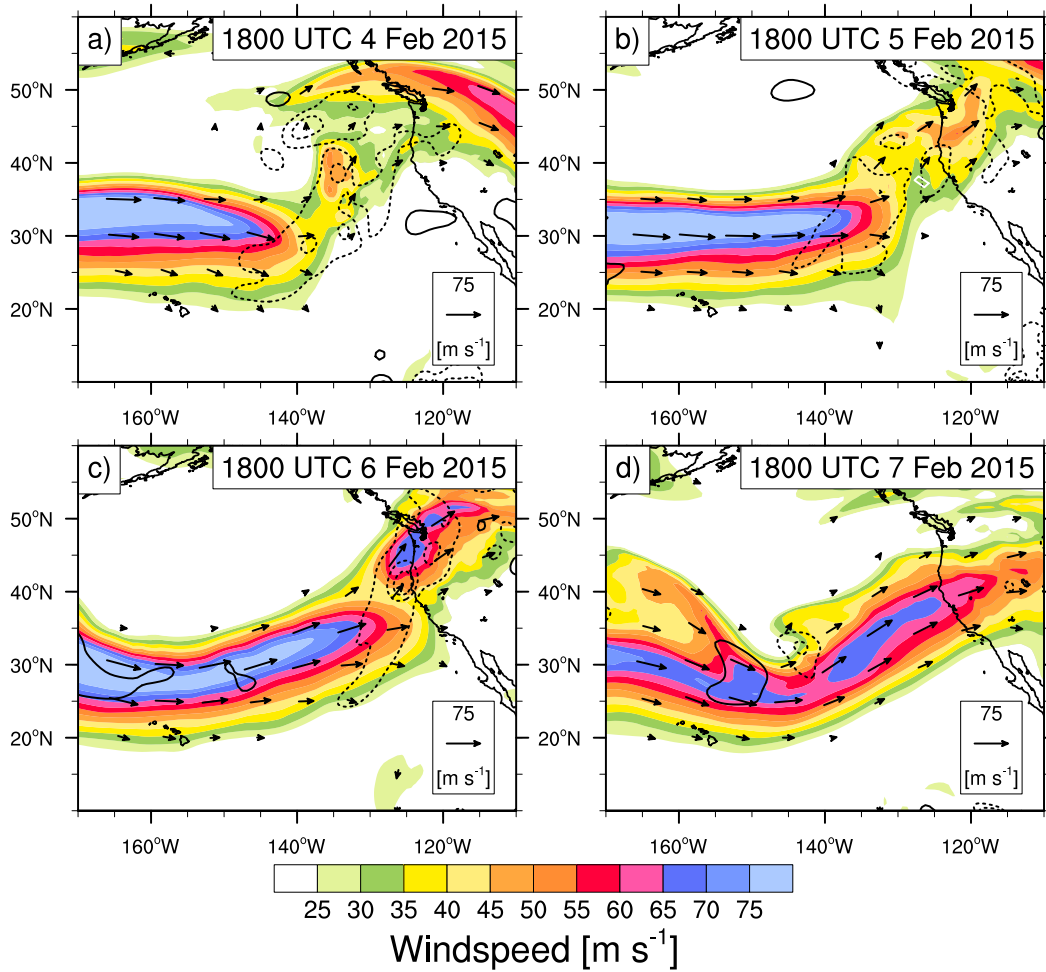


FIG. 5. As in Fig. 3, but from the MERRA-2 dataset for 300-hPa scalar wind (m s^{-1} ; color scale on bottom), 300-hPa wind velocity (vector scale at bottom right, for wind exceeding 25 m s^{-1}), and 300-hPa ω (plotted every 0.2 Pa s^{-1} , with solid black contours for positive, dashed black contours for negative, and no zero line). A 3×3 smoother was applied to wind and ω six times before plotting.

second term that is the column integral of water vapor change associated with dynamical convergence (CONV), as follows:

$$\frac{1}{g\rho_w} \int_{p_{\text{top}}}^{p_0} -\nabla \cdot (q\mathbf{V}) dp = \frac{1}{g\rho_w} \int_{p_{\text{top}}}^{p_0} (-\mathbf{V} \cdot \nabla q) dp + \frac{1}{g\rho_w} \int_{p_{\text{top}}}^{p_0} q(-\nabla \cdot \mathbf{V}) dp. \quad (2)$$

Using the continuity equation and the fact that pressure vertical velocity ω is negligible at the top of the column and is very small at the bottom of the column, CONV can be approximately represented as

$$\text{CONV} \approx \frac{1}{g\rho_w} \int_{p_{\text{top}}}^{p_0} \left(-\omega \frac{\partial q}{\partial p} \right) dp. \quad (3)$$

Here we see that CONV is related to vertical velocity (Wong et al. 2016), suggesting a close connection to precipitation when ascent occurs.

If the ADV and SFC terms are moved to the LHS of the water budget equation, it can be combined with the Eulerian IWV tendency to yield the Lagrangian IWV tendency (denoted by the subscript Lagr):

$$\frac{d\text{IWV}}{dt} \Big|_{\text{Lagr}} = \frac{\partial \text{IWV}}{\partial t} \Big|_{\text{Eul}} - \text{ADV} - \text{SFC} = \text{CONV} + E - P. \quad (4)$$

Here we neglect the second-order effects of vertical wind shear, which will have a small impact at hourly time scales since the troposphere is nearly barotropic (Fig. 6). The advantage of examining the water vapor budget in the frame of reference of a moving atmospheric column is that physical processes play the dominant role in changing IWV. It is more difficult to investigate the contribution of physical processes to IWV change at a fixed location due to the confounding impact of large-scale transport of water vapor.

TABLE 1. NOAA G-IV dropsonde information from flight on 5 Feb 2015. Boldface type indicates dropsondes that contribute to the water vapor budget region. Adjusted latitude and longitude are after time-to-space adjustment to a reference time of 1930 UTC.

Dropsonde No.	Time (UTC)	Lat (°N)	Lon (°W)	Adjusted lat	Adjusted long	IWV (mm)	IVT (kg m ⁻¹ s ⁻¹)
1	1836	35.24	122.02			9.5	103.4
2	1849	35.99	123.43			14.3	232.0
3	1903	36.84	125.05			25.2	584.5
4	1910	37.22	125.80	37.35	125.66	32.9	855.0
5	1916	37.71	126.52	37.74	126.49	27.0	977.4
6	1923	38.17	127.19	38.11	127.25	32.1	888.6
7	1927	37.86	127.47			Missing	Missing
8	1932	37.40	126.74	37.19	126.95	34.8	1054.8
9	1938	36.94	126.05	36.66	126.34	30.4	808.1
10	1943	36.66	126.38	36.29	126.77	32.2	877.5
11	1950	37.15	127.06	36.69	127.53	33.2	958.4
12	1956	37.62	127.74	37.07	128.30	33.8	1010.5
13	2002	38.11	128.42			30.2	877.9
14	2008	38.56	129.15			30.1	735.8
15	2027	38.16	127.14			33.5	1009.7
16	2034	38.63	127.86			33.6	992.6
17	2041	39.09	128.58			30.8	697.0
18	2048	39.70	129.39			28.4	731.8
19	2100	40.67	130.82			20.8	577.9
20	2113	41.59	132.32			14.7	362.9
21	2124	42.48	133.84			17.6	452.8
22	2136	43.29	135.46			21.1	284.5
23	2146	43.90	136.93			14.7	152.7
24	2154	43.10	137.30			18.8	168.4
25	2205	42.44	135.72			18.4	324.9
26	2215	41.82	134.10			16.8	424.1
27	2225	41.15	132.60			15.9	378.9
28	2236	40.43	131.05			17.1	378.2
29	2250	39.39	128.98			18.8	616.6
30	2257	38.84	127.98			28.7	740.2
31	2307	38.03	126.58			30.2	903.6
32	2318	37.18	125.14			27.6	654.7
33	2329	36.25	123.71			Missing	Missing
34	2340	35.41	122.33			13.2	187.2

b. Column-integrated moisture flux convergence

A region of the atmosphere over which a water vapor budget is calculated can be defined as the interior of a geometric prism with polygonal top and base defined by a set of dropsonde profiles at the vertices. Using the trapezoidal line-integral technique (McBride et al. 1989; Neiman et al. 2014), horizontal moisture flux convergence and dynamical convergence can be calculated at each level of the atmospheric prism as follows:

$$-\nabla \cdot (q\mathbf{V}) = -\frac{1}{A} \oint (qu \, dy - qv \, dx) \quad \text{and} \quad (5)$$

$$-\nabla \cdot \mathbf{V} = -\frac{1}{A} \oint (u \, dy - v \, dx), \quad (6)$$

where the path integral is calculated around the polygon with q , u , and v values obtained from dropsondes. The line integral technique yields quantitatively similar results to other methods (Bony and Stevens 2019). Horizontal moisture advection at each level can be obtained by subtracting the product of specific humidity and dynamical convergence from moisture flux convergence,

$$-\mathbf{V} \cdot \nabla q = -\nabla \cdot (q\mathbf{V}) - (-q\nabla \cdot \mathbf{V}) = -\frac{1}{A} \oint (qu \, dy - qv \, dx) + \frac{q}{A} \oint (u \, dy - v \, dx). \quad (7)$$

In the present study, dropsonde data were linearly interpolated to 1-hPa vertical spacing and integrated between the lowest surface pressure (999 hPa) and highest top pressure (198 hPa) among all budget region dropsondes.

Pressure vertical velocity ω was calculated by vertically integrating the horizontal divergence reported by the dropsondes. As a physical constraint, ω was required to have a value of zero at 198 hPa (in the stratosphere) and a value of ω_0 at 999 hPa (approximately the surface); this was accomplished by subtracting vertically averaged mass divergence from every level (mass balancing). The value ω_0 was determined as follows:

$$\omega_0 = \frac{\partial p_0}{\partial t} + \mathbf{V}_0 \cdot \nabla p_0 = \frac{\partial p_0}{\partial t} + g\rho_0 \mathbf{V}_0 \cdot \nabla Z_0.$$

Here, ρ_0 and Z_0 are density and geopotential height, respectively, on the bottom pressure surface, p_0 . The *RHB* reported a

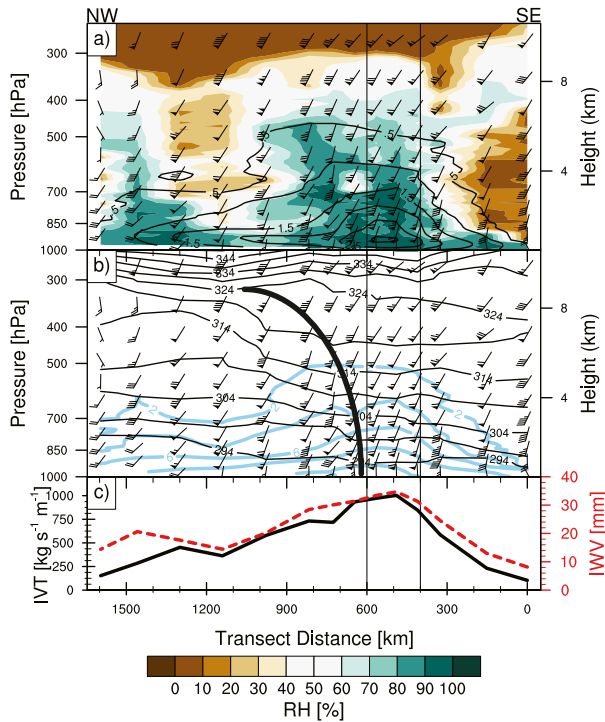


FIG. 6. G-IV dropsonde cross section along a NW-SE baseline parallel to the main G-IV flight track shown in Fig. 1: (a) relative humidity (%; color scale on bottom), horizontal wind (half barb 2.5 m s^{-1} , full barb 5 m s^{-1} , and pennant 25 m s^{-1}), and water vapor flux ($0.5 \text{ kg}^{-1} \text{ m}^{-1} \text{ s}^{-1} \text{ hPa}^{-1}$ interval; black contours); (b) potential temperature (5 K interval; black contours), horizontal wind [same as in (a)], and specific humidity (2 g kg^{-1} interval; blue contours); and (c) 1000–200-hPa IVT ($\text{kg}^{-1} \text{ s}^{-1} \text{ s}^{-1} \text{ hPa}^{-1}$; solid black) and IWV (mm; dashed red). The vertical lines denote the water vapor budget region, and the black curve in (b) denotes the approximate location of the cold front. A 3×3 smoother was applied to water vapor flux and specific humidity one time before plotting.

surface pressure tendency of -0.025 Pa s^{-1} during the dropsonde time period, which we assume is spatially representative of the entire water budget region. The advection term was obtained via the path integral of dropsonde measurements and, when combined with the pressure tendency, yielded a value of -0.053 Pa s^{-1} for ω_0 . After mass balancing was accomplished, values of CIMC, CONV, ADV, and SFC were calculated.

A necessary factor for determining whether the water vapor budget for a region can be closed is estimation of uncertainty for each term. For dropsonde observations, the two main sources of uncertainty are measurement uncertainty and sampling uncertainty (i.e., how representative the dropsonde profile is of the local environmental average). The dropsonde 2-sigma measurement uncertainties for wind velocity, temperature, and relative humidity are $\pm 0.5 \text{ m s}^{-1}$, $\pm 0.2^\circ\text{C}$, and $\pm 5\%$, respectively (Neiman et al. 2016; https://www.eol.ucar.edu/observing_facilities/avaps-dropsonde-system). An estimate of sampling uncertainty was obtained from the time series of in situ measurements made once per second by the

TABLE 2. Southeast-to-northwest sequence of profiles in cross section. Boldface type indicates dropsondes that contribute to the water vapor budget region.

Profile No.	Dropsondes
1	1
2	2
3	3
4	Avg of 4 , 9 , and 10
5	Avg of 5 , 8 , and 11
6	Avg of 6 , 12 , and 15
7	Avg of 13 and 16
8	Avg of 14 and 17
9	18
10	19
11	20
12	21
13	22
14	23

NOAA P-3 as it flew through the budget region at an elevation of 2400 m (in the lower troposphere where moisture flux is largest). Each of the three P-3 legs was split into two segments each about 100 km long (approximately the distance between two dropsondes). The time series for each segment were detrended, and the standard deviations of the measured values across all segments were 1.1 m s^{-1} , 0.2 K , and 4.5% for wind velocity, temperature, and relative humidity, respectively. These were deemed the 1-sigma sampling uncertainty for the respective meteorological variables. In the absence of other information, we assume this sampling uncertainty applies at all pressure levels.

Without knowing the vertical decorrelation scale, it is a nontrivial task to determine column integral uncertainties using formal methods, so a Monte Carlo approach was adopted instead. To each measurement in the original profile of each dropsonde, two random numbers were added. The first random number was drawn from a 0-mean normal distribution with standard deviation equal to the 1-sigma measurement uncertainty, and the second random number was drawn from a 0-mean normal distribution with standard deviation equal to the 1-sigma sampling uncertainty. The values of CIMC, CONV, ADV, and SFC were calculated, and the process was repeated 1000 times. The resulting 1000 CIMC, CONV, ADV, and SFC values were sequentially ranked, and the 2-sigma (95%) uncertainty range was determined as the range between the 25th and 975th values.

c. Precipitation

Precipitation in a water vapor budget region can be estimated from aircraft radar measurements. In the present study, we employ along-track reflectivity from the G-IV TDR measured over the three flight segments displayed Fig. 8. Only data within 30 km of the aircraft were used to reduce the effect of beam broadening caused by large beamwidth. Similar to Neiman et al. (2016, 2017), ground clutter and sidelobe effects were manually removed before interpolating reflectivity values onto a Cartesian grid with 1-km horizontal resolution and

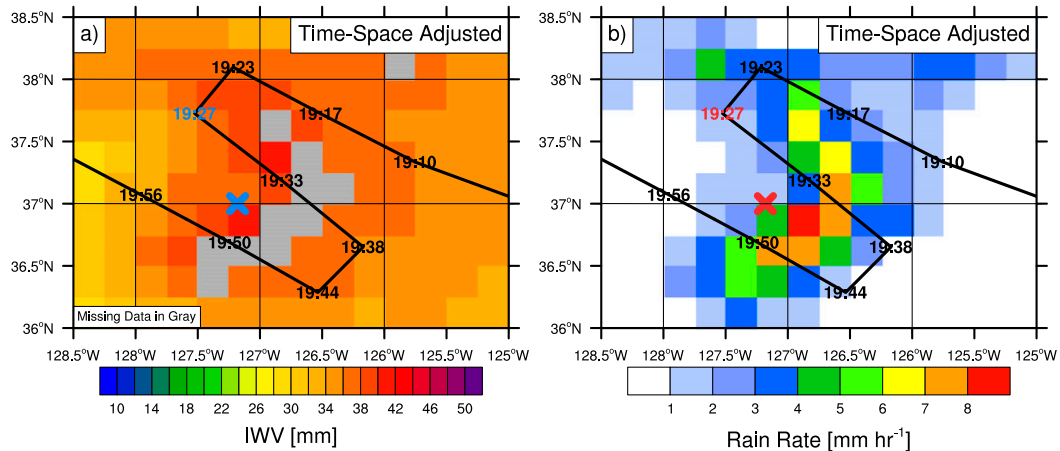


FIG. 7. Satellite SSMIS imagery from 1615 UTC 5 Feb 2015 after time-to-space adjustment to 1930 UTC for (a) IWV (mm; color scale at bottom, with gray for missing data) and (b) rain rate (mm h^{-1} ; color scale at bottom). In (a) and (b) the G-IV flight track and dropsonde positions after time-to-space adjustment are superimposed and labeled with their release times. The location of the *RHB* is marked by the “x”, and dropsonde 7 released at 1927 UTC is labeled with a different color to indicate it had missing data. The flight path proceeds from right to left and extends beyond the plot domain.

0.25-km vertical resolution. Due to sea surface clutter and beam broadening, reflectivity data below 1-km elevation lack consistently good quality across the entire 60-km-wide G-IV swath. Therefore, surface rain rate was estimated from mean reflectivity in the 1.0–1.5-km elevation interval. Considering that the atmosphere is nearly saturated below 1-km elevation (Fig. 9), we expect that precipitation at 1 km will be representative of precipitation reaching the surface.

Conversion of radar reflectivity to rain rate requires the application of an empirically derived reflectivity–rain-rate (Z – R) relationship (e.g., Marshall and Palmer 1948). The Z – R relationship is conventionally represented by the equation $Z = aR^b$, which includes parameters a and b to account for variations in precipitation for a given reflectivity arising from differences in the drop size distribution. Because of the lack of previous studies investigating Z – R relationships in AR conditions over the eastern Pacific, there are no standard a and b parameters to apply to the reflectivity data analyzed here. A further complication is rapid spatiotemporal evolution of drop size distributions in ARs (Martner et al. 2008; Neiman et al. 2017). Thus, two separate approaches were used to estimate rain rate from the TDR reflectivity. The first was the application of several well-known and previously published Z – R relationships to the gridded reflectivity values. Table 3 lists the different Z – R relationships and the general conditions for which they are suitable, none of which correspond to oceanic ARs. The second approach was the application of a Z – R relationship derived from disdrometer measurements made on board the *RHB* in the water vapor budget region on the same day as the G-IV flight. One additional step was application of the various Z – R relationships used in this study according to whether the precipitation in each 1-km horizontal grid box was classified as convective or stratiform. The occurrence of convective or stratiform precipitation was identified from gradients in the vertical profile of radar reflectivity using a method

similar to the algorithm for processing Tropical Rainfall Measurement Mission satellite radar data (Awaka et al. 1997).

The primary Z – R relationship used in this study is derived from 1-min averages of dBZ and R measured by the *RHB* disdrometer on 5 February 2015, all occurring in the prefrontal AR and almost all of them for the time period after 1130 UTC. We believe these data best characterize the raindrop distribution sampled by the G-IV TDR during 1900–2000 UTC on the same day. A conventional linear regression was calculated using dBZ as the independent variable and $\log_{10}R$ as the dependent variable; the data were very linear in log–log space. The resulting slope and intercept were converted to conventional a and b parameters, and uncertainties were propagated using formal methods. One key factor in determining the uncertainty in R is the effective sample size of the disdrometer measurements. Using the lag-1 autocorrelation method for covarying parameters (Bretherton et al. 1999), we estimate 2.33 min occur between independent measurements (i.e., the effective sample size is only 43% of the nominal sample size). This time interval corresponds to a distance of about 4 km for an advection velocity of 30 m s^{-1} , which appears to be about the scale of precipitation features apparent in Fig. 8. The disdrometer-derived relationship was applied only to stratiform precipitation. Some convective cells may have been sampled by the disdrometer, but with only surface information it was not possible to exclude those.

Several potential sources of uncertainty in area-averaged rain rate include 1) radar reflectivity measurement errors, 2) uncertainties associated with not sampling the entire budget region, and 3) uncertainties in the disdrometer measurements and the conversion of radar reflectivity to rain rate. Concerning the first, we assume that no systematic bias is present in the G-IV TDR reflectivity measurements since we have no means of determining otherwise, and furthermore note that random errors will average out in the area mean. Concerning the second, we assume that the probability distribution of precipitation

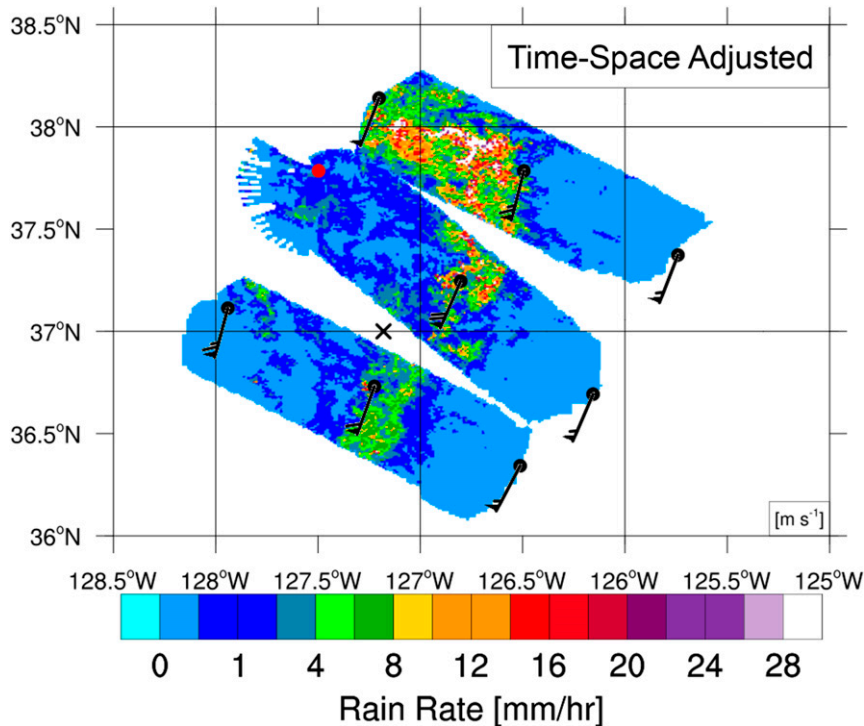


FIG. 8. Plan view of decluttered and Cartesian-gridded radar-derived rain rate at 1–1.5 km MSL from the NOAA G-IV TDR after time-to-space adjustment to 1930 UTC (mm h^{-1} ; color scale at bottom, with gray indicating no radar coverage). The G-IV dropsonde positions after time-to-space adjustment are superimposed and indicate 925-hPa wind (half barb 2.5 m s^{-1} , full barb 5 m s^{-1} , and pennant 25 m s^{-1}). The location of the *RHB* is marked by the “x,” and dropsonde 7 is labeled in red to indicate it had missing data.

values in the unsampled part of a budget region is the same as it is in the sampled part; if so, Monte Carlo tests indicate uncertainty due to undersampling will be small when the majority of the region has radar coverage. Concerning the third, we note that the *RHB* disdrometer reported about 40% less precipitation on average than the other instruments on the ship. Since the magnitude of the underestimate was not uniform across time or weather conditions, it was infeasible to apply a correction to disdrometer measurements. Instead, we assume that the *RHB* disdrometer measurements accurately characterize the Z – R relationship and that the only uncertainty arises from the fit to the data. An alternative assessment of uncertainty is provided by the spread in rain rate obtained from several previously published Z – R relationships. Conversion of radar reflectivity to rain rate is the dominant uncertainty in area-averaged rain rate.

d. Evaporation

Evaporation in a water vapor budget region can be estimated from reanalysis surface wind, temperature, and humidity using a bulk formula (Fairall et al. 1996, 2003; Peng et al. 2013) or obtained from in situ measurements by the *RHB* (Neiman et al. 2017). Uncertainty can be assessed as the RMS difference between evaporation values obtained from the two methods during a time period when the *RHB* was in prefrontal AR conditions.

e. Time-difference IWV tendency

The IWV time tendency can be directly determined by calculating the difference between IWV reported at two different times and then dividing by the difference in time. We refer to this as time-difference IWV tendency to distinguish it from the instantaneous IWV tendency obtained as the sum of moisture convergence, precipitation, and evaporation terms. In the present study, IWV retrieved by satellite at an earlier time was interpolated to dropsonde locations. Then the difference between satellite and dropsonde IWV was averaged over all dropsondes in a water vapor budget region. According to the 1535 UTC overpass of the *F17* satellite and ignoring potential retrieval bias, the reported 2-sigma uncertainty for IWV in this region of the prefrontal AR was 0.8 mm ; we assumed the same uncertainty applied to the 1615 UTC overpass of the *F18* satellite which does not provide an uncertainty estimate. Uncertainty in dropsonde IWV was obtained from the previously described Monte Carlo method and combined with the satellite uncertainty to get total uncertainty for the time-difference IWV tendency.

f. Time-to-space adjustment

Since the G-IV took about 50 min to measure the water vapor budget region and the budget calculation requires simultaneous observations, the present study applied time-to-space adjustment

Budget Region Dropsonde Vertical Profiles

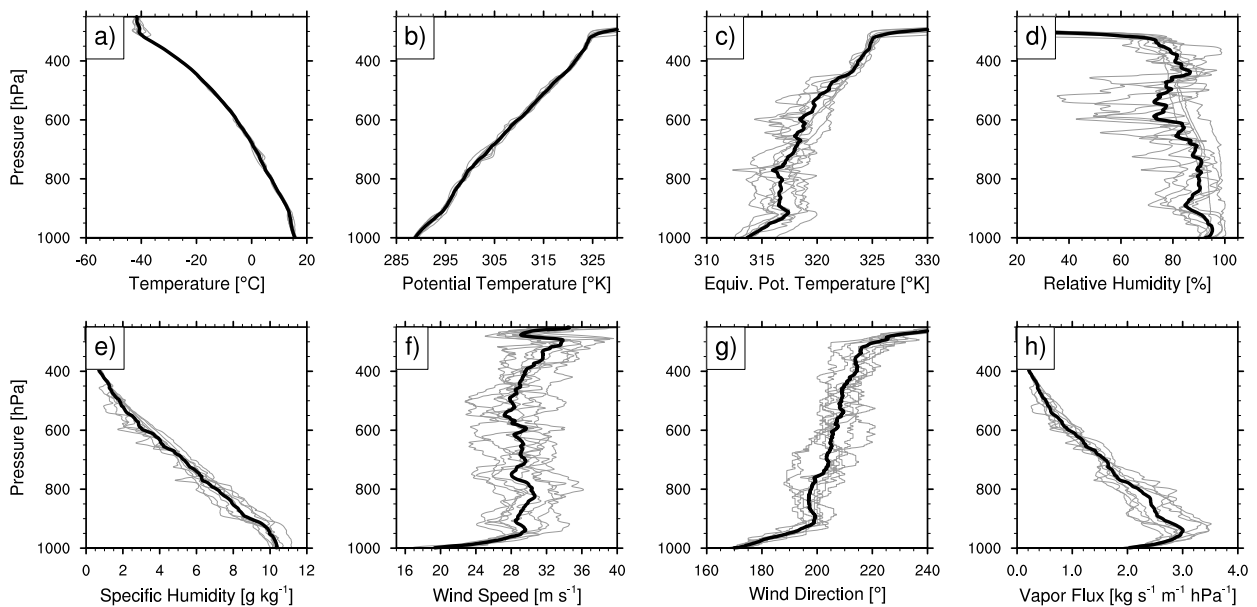


FIG. 9. Vertical profiles for the eight G-IV dropsondes in the water vapor budget region (4, 5, 6, 8, 9, 10, 11, and 12) plotted for individual dropsondes (thin curves) and averaged over all dropsondes (thick curves) for (a) temperature ($^{\circ}\text{C}$), (b) potential temperature (K), (c) equivalent potential temperature (K), (d) relative humidity (%), (e) specific humidity (g kg^{-1}), (f) wind speed (m s^{-1}), (g) wind direction ($^{\circ}$), and (h) moisture flux ($\text{kg m}^{-1} \text{s}^{-1} \text{hPa}^{-1}$).

so that each radar and dropsonde measurement was located at the putative position where the sampled atmospheric volume was at the reference time of 1930 UTC, assuming all atmospheric volumes translate at the velocity of the AR. While radar measurements occurred instantaneously, dropsondes took about 15 min to fall to the surface, during which time they drifted a horizontal distance of about 24 km. Proper placement of dropsonde location with respect to the radar swaths is crucial in order to determine whether precipitation occurs inside or outside of a budget region (cf. Fig. 8 and online supplemental Fig. S2). In the absence of other information, we assumed that a dropsonde samples the same atmospheric column during its entire descent (i.e., the dropsonde falls vertically in the reference frame of the translating column). In that case, the time and location at which a dropsonde reaches the surface marks the sampled atmospheric column, to which time-to-space adjustment was then applied.

The velocity for time-to-space adjustment during the time period of the G-IV flight was assumed to be the vertically averaged horizontal wind measured by dropsonde and weighted according to moisture flux $q\mathbf{V}$ at each pressure level. Averaging across all eight dropsondes in the water vapor budget region yielded 28.2 m s^{-1} from 198° (zonal component = 8.6 m s^{-1} ; meridional component = 26.9 m s^{-1}). Moisture-flux weighted average velocity will be most representative of the translation velocity of column IWV. The calculations of moisture convergence, precipitation, and evaporation are not sensitive to the value of velocity employed for time-to-space adjustment because any error only slightly alters the polygonal geometry of the budget region and does not change the meteorological values on the vertices.

The calculation of the Lagrangian time-difference IWV tendency requires matching of a region in 1615 UTC satellite overpass with the region sampled by the G-IV dropsondes. Under the assumption that the general occurrence of precipitation within an $\sim 200 \text{ km} \times 200 \text{ km}$ atmospheric column will persist over 4 h even as individual precipitating elements arise and dissipate, we identified the area within the entire satellite swath that exhibited a pattern of rain rate with the highest spatial correlation to the pattern of precipitation estimated from the G-IV TDR. The velocity for time-to-space adjustment between the 1615 UTC satellite overpass and the 1930 UTC reference time was determined according to the geographical displacement between the satellite rain rate imagery and the radar precipitation pattern, yielding 35.9 m s^{-1} from 219° (zonal component = 22.7 m s^{-1} and meridional component = 27.8 m s^{-1}). We do not expect exact agreement between the AR translation velocity determined by dropsonde wind and by satellite-radar pattern matching because of their different time periods, but the general similarity between values obtained from the two independent methods is encouraging. Note that the Lagrangian time-difference IWV tendency is sensitive to the value of velocity for time-to-space adjustment because the time interval between the satellite overpass and the G-IV flight is nearly 4 h and employing a different velocity brings a different area of the satellite swath to the budget region.

g. Specific water vapor budget regions

Figure 10 displays the specific water vapor budget regions examined in the present study, and Table 4 lists the dropsonde

TABLE 3. Reflectivity–rain rate relationships used in this study. Boldface type indicates a primary relationship.

$Z = aR^b$	Source	Applicable conditions	Separate convective
$Z = 300R^{1.4}$	WSR88 convective (Hunter 1996)	Summer convective precipitation	None
$Z = 200R^{1.66}$	Marshall and Palmer (1948)	General stratiform precipitation	None
$Z = 200R^{1.66}$	Marshall and Palmer (1948)	General stratiform precipitation	WSR88
$Z = 360R^{1.41}$	Meneghini and Kozu (1990)	General stratiform precipitation	None
$Z = 360R^{1.41}$	Meneghini and Kozu (1990)	General stratiform precipitation	WSR88
$Z = 168R^{1.58}$	Martner et al. (2008)	West Coast stratiform brightband precipitation	None
$Z = 168R^{1.58}$	Martner et al. (2008)	West Coast stratiform brightband precipitation	WSR88
$Z = 466R^{1.47}$	RHB disdrometer	AR in this study	WSR88

numbers for the polygonal vertices of each region. As in previous studies (Neiman et al. 2014, 2016), the entire area encompassed by the dropsondes is one budget region (B00), but the big budget region is additionally split into multiple, overlapping subregions bounded by various combinations of dropsondes (R01–R10). This enables investigation of smaller-scale spatial variability in water budget terms. Criteria for subregion selection out of all possible polygonal arrangements include compactness, no skipping over nearby dropsondes, and at least 55% radar area coverage.

6. Water budget results

a. Column-integrated moisture convergence and related components

Figure 11 displays the vertical profiles of $-\nabla \cdot (q\mathbf{V})$, $q(-\nabla \cdot \mathbf{V})$, and $-\mathbf{V} \cdot \nabla q$, which, when integrated, yield CIMC, CONV, and ADV, respectively. The profile of pressure vertical velocity ω is also included. Profiles are shown for the entire budget region (B00), the subregion with most positive CIMC (R03), and the subregion with the most negative CIMC (R06). With the exception of a layer near 900 hPa, the entire budget region experiences increasing moisture from dynamical convergence in the lower troposphere, upward motion throughout the troposphere, and negligible horizontal moisture advection. The dominance of dynamical convergence over advection found in the present study is consistent with reanalysis results reported

by Guan et al. (2020) for the frontal sector of an AR. Relative to the entire budget region, the subregion with the most positive CIMC experiences 5 times as much moisture increase from dynamical convergence and 5 times as much upward motion. Although error bars are not included in the plots for readability, the differences between regions are caused by real spatial variability and not merely measurement and sampling uncertainty. Also note that the water budget in the present study is quantified over smaller areas than in previous studies (e.g., Neiman et al. 2014, 2016; Guan et al. 2020) and that the resulting terms have much larger magnitude than in those studies. The vertical integrals of Figs. 11a–c are listed in the CIMC, CONV, and ADV columns of Table 5, respectively, along with values for all the other subregions. The range of CIMC among subregions is substantial, varying from 10.0 mm h⁻¹ for R03 to -7.4 mm h⁻¹ for R06 and greatly exceeding the uncertainty of individual values. Nonetheless, this sizeable spatial variability largely averages out in the entire budget region since CIMC for B00 is only 0.7 mm h⁻¹.

CONV and ADV also span substantial ranges, albeit with CONV being mostly positive and ADV being mostly negative. Recalling that CIMC = CONV + ADV, Fig. 12 examines the separate contributions of CONV and ADV to CIMC. Here it is seen that the processes driving substantial positive and negative values of CIMC are not symmetrical. CIMC becomes substantially positive due to CONV with little contribution from ADV, as demonstrated by the nearness of CIMC–CONV

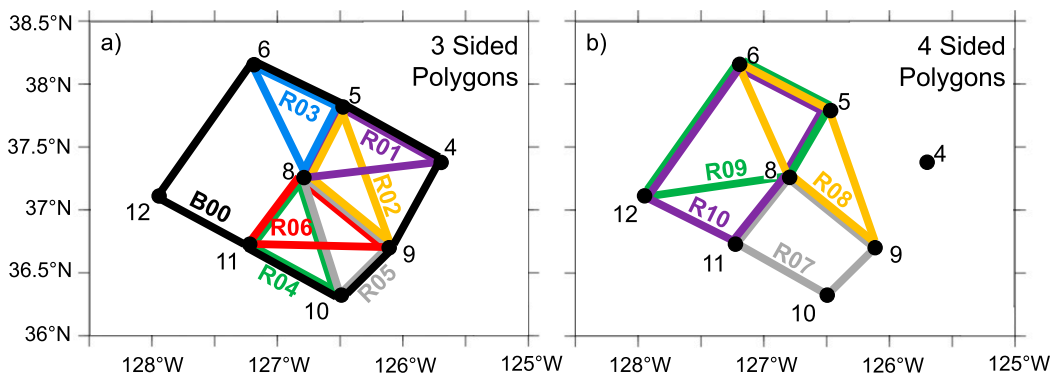


FIG. 10. Polygonal water vapor budget regions defined by numbered dropsondes at vertices: (a) entire budget region B00 (black) and subregions R01 (purple), R02 (yellow), R03 (blue), R04 (green), R05 (gray), and R06 (red) and (b) subregions R07 (gray), R08 (yellow), R09 (green), and R10 (purple).

TABLE 4. Water vapor budget regions.

Region identifier	Dropsondes	Fractional radar coverage
B00	4, 5, 6, 12, 11, 10, and 9	0.60
R01	4, 5, and 8	0.65
R02	5, 8, and 9	0.56
R03	5, 6, and 8	0.79
R04	8, 11, and 10	0.59
R05	8, 9, and 10	0.56
R06	8, 9, and 11	0.76
R07	8, 11, 10, and 9	0.57
R08	5, 6, 8, and 9	0.68
R09	5, 6, 12, and 8	0.76
R10	5, 6, 12, 11, and 8	0.68

points to the 1:1 line when CIMC is greater than 2 mm h^{-1} . Similarly, CIMC becomes substantially negative due to ADV with little contribution from CONV, as demonstrated by the nearness of CIMC-ADV points to the 1:1 line when CIMC is less than -2 mm h^{-1} . This asymmetry is likely driven by the physical environment of the AR. Strong downward motion is unlikely to occur, so vertical motion only acts in the direction of increasing moisture due to dynamical convergence in the lower troposphere. The atmosphere is already near saturation, so horizontal advection can only act in the direction of bringing drier air to the budget region.

As reported in Table 5, the magnitude of SFC is smaller than the magnitudes of CIMC, CONV, and ADV for all budget regions, and usually much smaller. This indicates that moisture flux through a tilted bottom pressure surface is generally not a substantial contributor to changes in IWV.

b. Precipitation and evaporation

Table 5 also lists area-average rain rate P for the entire budget region and all subregions. Here it is assumed that portions of a budget region without radar coverage have the same average rain rate as the portions with radar coverage. The fact that CONV can be recast in terms of vertical velocity

suggests there should be a close relationship between it and precipitation (e.g., [Cordeira et al. 2013](#)). Figure 13 bears out this conjecture. Irrespective of whether rain rate is estimated from radar reflectivity using a $Z-R$ relationship from the literature or one derived from the *RHB* disdrometer measurements, precipitation in a subregion increases proportionately to the value of positive CONV (and therefore proportionately to the magnitude of area-mean ascent, all else the same). For negative CONV, precipitation in a subregion is small (as would be expected for area-mean subsidence). The quantitative consistency between CONV and precipitation across budget regions provides confidence in the reliability of the two sets of independent measurements as well as our methods. It is also consistent with the near balance of reanalysis CONV and precipitation reported by [Guan et al. \(2020\)](#) for the frontal sector of an AR.

The subregion with most positive CIMC has a disdrometer-derived rain rate of 9.8 mm h^{-1} , the subregion with the most negative CIMC has a rain rate of 1.1 mm h^{-1} , and the entire budget region has a rain rate of 2.5 mm h^{-1} . Rain rates estimated from $Z-R$ relationships from the literature are uniformly higher than that from the disdrometer, perhaps due to underestimation of precipitation by the disdrometer, unique characteristics of this particular AR, or because relationships from the literature were derived for conditions other than oceanic ARs in general. Applying the disdrometer $Z-R$ relationship to convective as well as stratiform conditions would result in rain rates from 0 to 1.4 mm h^{-1} smaller than those reported in Table 5. Given the uncertainties in estimating rain rate from G-IV radar reflectivity and the *RHB* disdrometer, it is not possible to determine whether precipitation removes all, more than all, or less than all of the increase in moisture produced by dynamical convergence.

According to both *RHB* in situ measurements and reanalysis products, evaporation during the 6 h period around the time of the G-IV flight was less than 0.1 mm h^{-1} across the entire budget region. Despite the strong surface wind speed, the very high relative humidity near the surface suppressed evaporation. Therefore, the source of moisture for the AR is not local.

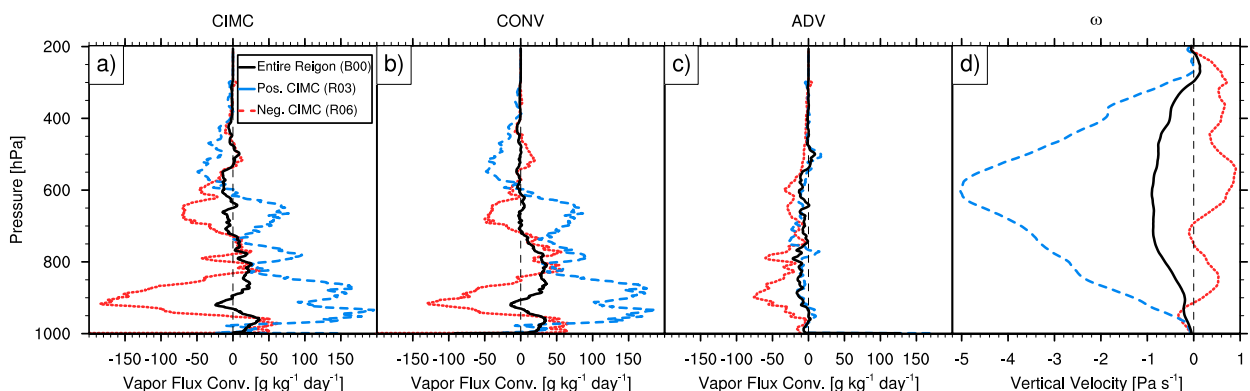


FIG. 11. Kinematic diagnostic profiles derived from the G-IV dropsondes composing the entire budget region (B00; black) and subregions with the most positive CIMC (R03; dashed blue) and most negative CIMC (R06; dotted red), as defined in Fig. 10 and Table 4: (a) mass-balanced horizontal moisture convergence ($\text{g kg}^{-1} \text{ day}^{-1}$), (b) mass-balanced change in moisture from horizontal dynamical convergence ($\text{g kg}^{-1} \text{ day}^{-1}$), (c) mass-balanced horizontal moisture advection ($\text{g kg}^{-1} \text{ day}^{-1}$), and (d) pressure vertical velocity (Pa s^{-1}).

TABLE 5. Individual water vapor budget terms (mm h^{-1}). Numbers in parentheses span 2-sigma (95%) uncertainty.

Region identifier	CIMC	ADV	CONV	SFC	P^a	E
B00	0.7 (0.5, 0.9)	-1.5 (-1.6, -1.3)	2.2 (2.1, 2.3)	-0.1 (-0.1, -0.1)	2.5 (2.1, 2.9)	0.0
R01	0.9 (-0.1, 1.6)	-2.3 (-3.1, -1.5)	3.2 (2.7, 3.4)	-0.7 (-0.7, -0.6)	1.7 (1.4, 2.0)	0.0
R02	5.8 (4.8, 6.4)	-0.6 (-1.4, 0.0)	6.4 (5.9, 6.7)	-0.3 (-0.3, -0.2)	2.7 (2.3, 3.1)	0.0
R03 ^b	10.0 (9.1, 10.7)	-1.3 (-1.9, -0.5)	11.3 (10.8, 11.6)	-0.2 (-0.2, -0.2)	9.8 (7.9, 11.7)	0.0
R04	-5.4 (-5.8, -4.8)	-4.8 (-5.2, -4.3)	-0.6 (-0.8, -0.3)	-0.1 (-0.1, -0.1)	1.2 (1.1, 1.3)	0.0
R05	3.0 (2.2, 3.4)	3.0 (2.3, 3.3)	0.0 (-0.3, 0.4)	0.0 (-0.1, 0.0)	0.5 (0.4, 0.6)	0.0
R06 ^c	-7.4 (-8.0, -6.9)	-5.9 (-6.5, -5.4)	-1.5 (-1.8, -1.3)	-0.2 (-0.2, -0.1)	1.1 (1.0, 1.2)	0.0
R07	-1.6 (-2.0, -1.2)	-1.3 (-1.6, -0.9)	-0.3 (-0.5, -0.1)	-0.1 (-0.1, -0.1)	1.0 (0.9, 1.1)	0.0
R08	6.9 (6.2, 7.5)	-1.6 (-2.2, -0.9)	8.5 (8.1, 8.7)	-0.2 (-0.2, -0.2)	6.5 (5.2, 7.8)	0.0
R09	7.1 (6.7, 7.4)	1.2 (0.9, 1.5)	5.9 (5.7, 6.0)	-0.2 (-0.2, -0.1)	4.5 (3.7, 5.3)	0.0
R10	3.2 (2.9, 3.4)	-0.4 (-0.5, -0.1)	3.6 (3.4, 3.7)	-0.2 (-0.2, -0.2)	3.8 (3.1, 4.5)	0.0

^a Uncertainty derived from fit to disdrometer data.

^b Region with most positive CIMC.

^c Region with most negative CIMC.

Guan et al. (2020) also report that evaporation is negligible in the frontal and prefrontal sectors of an AR. Since the uncertainty of evaporation is also less than 0.1 mm h^{-1} , the evaporation term is left out of budget calculations.

c. Integrated water vapor tendency

Instantaneous values of IWV tendency in the Lagrangian and Eulerian frames of reference can be obtained by subtracting precipitation from CONV and by subtracting precipitation from the sum of CIMC and SFC, respectively. These can be compared with values of IWV tendency calculated from the difference in IWV between dropsondes and a prior satellite pass with time-to-space adjustment (Lagrangian) or without (Eulerian). Table 6 lists the results and Fig. 14 displays the results for the entire budget region and subregions. The time-difference IWV tendencies for the entire budget region are -1.2 and -0.5 mm h^{-1} for Lagrangian and Eulerian frames, respectively. This rate of decrease is generally consistent with the overall rate of IWV decrease observed between 4 and 7 February 2015 in satellite imagery displayed in Fig. 2. Time-difference tendencies for subregions range between -0.1 and -1.7 mm h^{-1} . The similarity between Lagrangian and Eulerian values of time-difference IWV tendency is consistent with temporally averaged advection occurring primarily in the along-AR direction and with IWV having little spatially averaged change across 400 km in the along-AR direction. Although within the range of uncertainty, the slightly smaller IWV tendency for the Eulerian frame suggests that about 0.7 mm h^{-1} advective moistening occurred in the entire budget region from 1615 to 1930 UTC. These results are consistent with those of Guan et al. (2020), who reported slight advective moistening but negative Eulerian IWV tendency as average reanalysis conditions for the frontal sector of an AR.

Values of instantaneous IWV tendency exhibit a much larger range across the budget subregions than do values of time-difference IWV tendency. This is not surprising since the latter represent an average over time that smooths out higher variability occurring at shorter time scales. Similarly, the instantaneous IWV tendency for the entire budget region is smaller than the instantaneous IWV tendencies for most subregions because

spatially averaging over the entire budget region smooths out higher variability occurring at smaller spatial scales. Although there is no reason to expect that an instantaneous tendency will be commensurate with a time-averaged tendency, the fact that many subregions have instantaneous tendencies with magnitudes several times larger than the time-difference tendencies indicates that the physical processes producing the large instantaneous tendencies are not sustained over periods longer than about an hour; otherwise, the time-difference IWV tendencies would be greater than observed.

Budget subregions R04 and R06 exhibit especially large negative instantaneous IWV tendency in the Eulerian frame (Table 6 reports -6.5 and -8.3 mm h^{-1} , respectively) but not in the Lagrangian frame (only -1.8 and -2.6 mm h^{-1} , respectively). This is driven by small-scale strong advective drying (Table 5 reports -4.8 and -5.9 mm h^{-1} , respectively). Other subregions do not have equivalently large positive values in Eulerian instantaneous IWV tendency (R02 has a value of only 3.4 mm h^{-1}). This asymmetry in Eulerian instantaneous IWV tendency arises from the different processes driving positive and negative

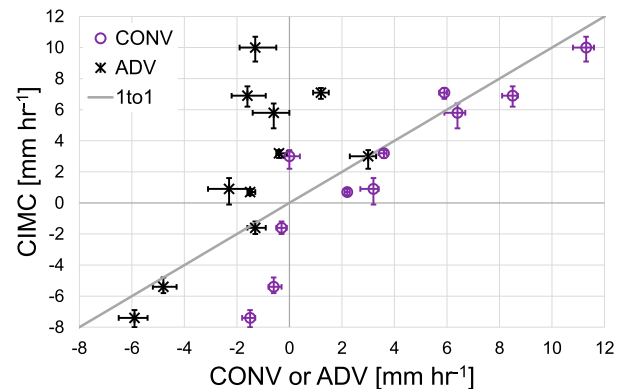


FIG. 12. Scatterplot of CIMC (mm h^{-1}) plotted against moisture change from dynamical convergence (CONV; purple circles; mm h^{-1}) or moisture change from advection (ADV; black "x"; mm h^{-1}) for the entire budget region and each subregion, as defined in Fig. 10 and Table 4. Error bars indicate the 2-sigma (95%) uncertainty range.

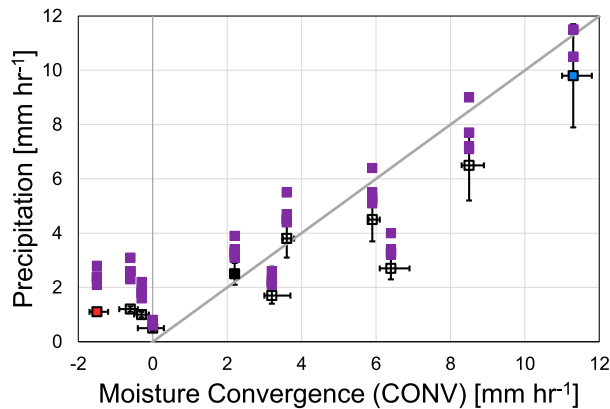


FIG. 13. Scatterplot of rain rate (mm h^{-1}) derived from Z - R relationships from the literature (purple squares) and RHB disdrometer (nonpurple squares) plotted against moisture change from $CONV$ (mm h^{-1}) for the entire budget region and each subregion, as defined in Fig. 10 and Table 4. Filled black, blue, and red squares indicate the entire budget region and subregions with most positive and negative CIMC (B00, R03, and R06, respectively). Error bars indicate the 2-sigma (95%) uncertainty range.

IWV tendency. Localized strong dynamical convergence in the lower troposphere enhances IWV, but conditions of near saturation generate precipitation that quickly removes moisture and thereby limits how much IWV can increase. Contrastingly, localized dry advection reduces IWV, but there is no compensating process that will quickly moisten the atmosphere and limit how much IWV can decrease.

d. Water vapor budget closure

Recalling that instantaneous IWV tendency is the sum of observed precipitation, evaporation, and moisture convergence through column sides and bottom, the subtraction of observed time-difference IWV tendency from instantaneous IWV tendency should result in a total budget value of zero if the water vapor budget is closed and the two methods for

observing tendency are both accurate and commensurate. Hence, the closer points in Fig. 14 are to the 1:1 line when considering the uncertainty ranges, the closer those regions are to budget closure. Table 6 shows total budget values with 2-sigma (95%) uncertainty ranges for the entire budget region and all subregions in the Lagrangian and Eulerian reference frames. The main sources of potential inaccuracy not represented in the given uncertainty ranges are lack of calibration of the G-IV TDR and/or use of an unsuitable Z - R relationship. This could produce a bias in the estimated rain rate, but it is unlikely that such a bias would rise to the same magnitude as the large total budget deviations from zero that occur for several subregions. Instead, it is more likely that the lack of budget closure arises from the incommensurate time scales of the instantaneous IWV tendency and the time-difference IWV tendency. An additional source of potential inaccuracy for the Lagrangian time-difference IWV tendency is possible misidentification of the region in 1615 UTC satellite overpass that moved to the location sampled by the G-IV dropsondes at 1930 UTC. However, the fact that the Eulerian total budget is farther from closure than the Lagrangian total budget suggests that satellite pattern mismatching is unlikely to be a major contributor to lack of closure.

Examining the entire budget region B00, we see that dynamical convergence ($CONV$) causes IWV to increase by 2.2 mm h^{-1} while precipitation reduces IWV by 2.5 mm h^{-1} , resulting in a Lagrangian instantaneous IWV tendency equal to $-0.3 \pm 0.4 \text{ mm h}^{-1}$ (Tables 5 and 6). Since the Lagrangian time-difference IWV tendency is $-1.2 \pm 0.8 \text{ mm h}^{-1}$, it appears that the water vapor budget is not quite observationally closed in the reference frame of a translating atmospheric column. One possibility is that the rain rate derived from the RHB disdrometer Z - R relationship is biased low and use of a different precipitation estimate from Fig. 13 would result in budget closure. Another possibility is that the observed instantaneous IWV tendency is not fully representative of the actual IWV tendency over several hours. The uncertainty associated with temporal representativeness can be estimated by dividing the total budget region into eight nonoverlapping

TABLE 6. Lagrangian and Eulerian IWV tendencies (mm h^{-1}). Numbers in parentheses span 2-sigma (95%) uncertainty.

Region identifier	Lagrangian total budget	Lagrangian time-difference IWV tendency	Lagrangian instantaneous IWV tendency	Eulerian total budget	Eulerian time-difference IWV tendency	Eulerian instantaneous IWV tendency
B00	0.9 (0.5, 1.3)	-1.2 (-1.4, -1.0)	-0.3 (-0.7, 0.1)	-1.2 (-1.6, -0.8)	-0.5 (-0.7, -0.3)	-1.7 (-2.1, -1.3)
R01	2.6 (1.9, 3.1)	-1.1 (-1.4, -0.8)	1.5 (0.9, 1.9)	0.0 (-1.0, 0.9)	-0.1 (-0.4, 0.2)	-0.1 (-1.1, 0.7)
R02	5.1 (4.5, 5.6)	-1.4 (-1.6, -1.2)	3.7 (3.1, 4.2)	3.8 (2.7, 4.5)	-0.4 (-0.6, -0.2)	3.4 (2.3, 4.1)
R03 ^a	2.8 (0.8, 4.7)	-1.3 (-1.6, -1.0)	1.5 (-0.5, 3.4)	0.6 (-1.5, 2.6)	-0.2 (-0.5, 0.1)	0.4 (-1.7, 2.4)
R04	-0.3 (-0.6, 0.1)	-1.5 (-1.7, -1.3)	-1.8 (-2.0, -1.5)	-5.9 (-6.3, -5.3)	-0.6 (-0.8, -0.4)	-6.5 (-6.9, -5.9)
R05	1.1 (0.7, 1.5)	-1.6 (-1.8, -1.4)	-0.5 (-0.8, -0.1)	3.2 (2.4, 3.6)	-0.7 (-0.9, -0.5)	2.5 (1.7, 2.9)
R06 ^b	-0.9 (-1.3, -0.6)	-1.7 (-1.9, -1.5)	-2.6 (-2.9, -2.4)	-7.5 (-8.1, -7.0)	-0.8 (-1.0, -0.6)	-8.3 (-8.9, -7.8)
R07	0.3 (0.0, 0.6)	-1.6 (-1.8, -1.4)	-1.3 (-1.5, -1.1)	-1.7 (-2.1, -1.3)	-0.8 (-1.0, -0.6)	-2.5 (-2.9, -2.1)
R08	3.4 (2.0, 4.7)	-1.4 (-1.6, -1.2)	2.0 (0.6, 3.3)	1.1 (-0.4, 2.5)	-0.5 (-0.7, -0.3)	0.6 (-0.9, 2.0)
R09	2.4 (1.6, 3.2)	-1.0 (-1.2, -0.8)	1.4 (0.6, 2.2)	3.0 (2.1, 3.9)	-0.2 (-0.4, 0.0)	2.8 (1.9, 3.7)
R10	0.9 (0.2, 1.6)	-1.1 (-1.3, -0.9)	-0.2 (-0.9, 0.5)	0.0 (-0.8, 0.7)	-0.4 (-0.6, -0.2)	-0.4 (-1.2, 0.3)

^a Region with most positive CIMC.

^b Region with most negative CIMC.

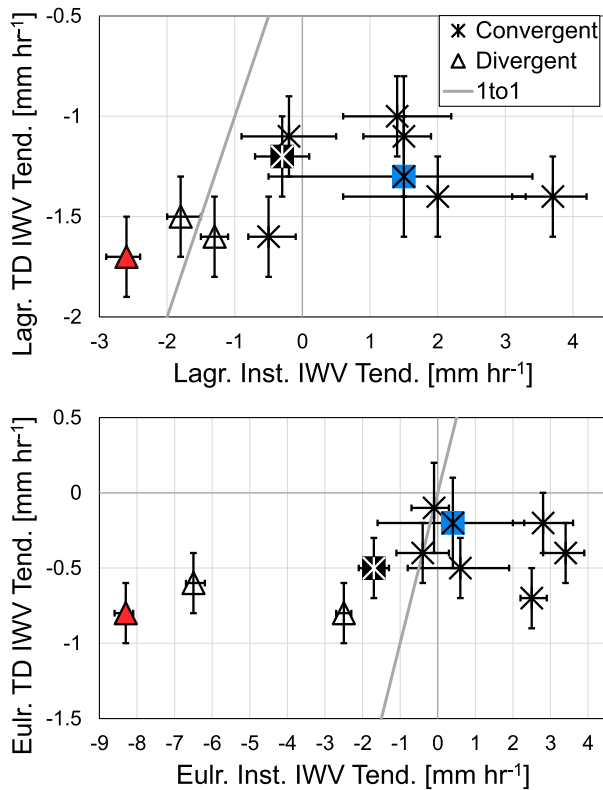


FIG. 14. Scatterplot of time-difference IWV tendency (mm h^{-1}) determined from the difference in IWV between dropsondes at 1930 UTC and a satellite pass at 1615 UTC plotted against instantaneous IWV tendency (mm h^{-1}) determined from the difference between moisture convergence and precipitation at 1930 UTC for the entire budget region and each subregion, as defined in Fig. 10 and Table 4: (a) Lagrangian reference frame with time-to-space adjustment applied to the satellite data and moisture convergence calculated only from dynamical convergence and (b) Eulerian reference frame with no time-to-space adjustment applied to the satellite data and moisture convergence calculated from dynamical convergence and advection. Filled black, blue, and red symbols indicate the entire budget region and subregions with most positive and negative CIMC (B00, R03, and R06, respectively). Error bars indicate the 2-sigma (95%) uncertainty range.

subregions and assuming that the set of subregion instantaneous IWV tendency values comprise the distribution of subregion conditions that can possibly occur. Monte Carlo sampling with replacement from this distribution and accumulation of the values until the total area of the full budget region is reached yields an alternative possible value for the instantaneous IWV tendency. Repeating this 10 000 times provides a distribution of possible instantaneous IWV tendency values from which we obtain a 95% uncertainty range that spans the interval from -1.9 to 1.0 mm h^{-1} . This interval includes the time-difference IWV tendency and brings budget closure for the entire budget region B00.

Different values of IWV tendency occur for the entire budget region in the Eulerian reference frame. Advective drying (ADV) and moisture flux through the tilted bottom pressure surface (SFC) cause IWV to decrease by 1.5 and

0.1 mm h^{-1} , respectively, resulting in an Eulerian instantaneous IWV tendency equal to $-1.7 \pm 0.4 \text{ mm h}^{-1}$. Since the Eulerian time-difference IWV tendency for B00 is only $-0.5 \pm 0.6 \text{ mm h}^{-1}$, the water vapor budget again appears to be observationally unclosed. Unlike the Lagrangian case, use of a different precipitation estimate from Fig. 13 would increase precipitation loss and lack of closure. However, a Monte Carlo estimate of 95% uncertainty range associated with temporal representativeness spans the large interval from -5.4 to 1.1 mm h^{-1} , which includes the time-difference IWV tendency and brings budget closure. These results suggest that variability in moisture advection on short time scales can have a confounding influence on aircraft measurements of the water vapor budget. For this reason, it may be preferable to investigate the water vapor budget in the reference frame of a translating atmospheric column so that only the effects of dynamical convergence and precipitation need be considered.

7. Conclusions

This study combined airborne, shipboard, and satellite measurements to provide the first observational assessment of all major terms of the IWV budget for a $150 \text{ km} \times 160 \text{ km}$ region within the core of a strong atmospheric river over the northeast Pacific. As in previous work, column-integrated moisture flux convergence was estimated from dropsonde profiles, but the present study additionally split column-integrated moisture flux convergence into a component associated with horizontal advection and a component associated with dynamical convergence and vertical motion. Advection transports IWV from one location to another but does not change IWV within the moving column, whereas low-level dynamical convergence acts to increase IWV and generate upward motion. The dropsonde observations occurring around 1930 UTC 5 February 2015 indicate that advection of drier air into the budget region ($-1.50 \pm 0.21 \text{ mm h}^{-1}$) offset a large fraction of the increase in IWV due to dynamical convergence ($2.20 \pm 0.12 \text{ mm h}^{-1}$). One innovation of the present study was observationally estimating precipitation by conversion of NOAA G-IV tail Doppler radar reflectivity to rain rate using a $Z-R$ relationship derived from shipboard disdrometer measurements on the same day. Precipitation reduced IWV in the budget region by an amount ($-2.47 \pm 0.41 \text{ mm h}^{-1}$) slightly exceeding the increase from dynamical convergence. Use of a $Z-R$ relationship from the published literature (and for conditions other than an oceanic AR) would yield higher rain rates than above and may be more realistic considering that the shipboard disdrometer underestimated precipitation relative to other instruments by about 40% on average. Due to the extremely high relative humidity of the lower troposphere, surface evaporation made no contribution to changing IWV ($0.0 \pm 0.05 \text{ mm h}^{-1}$).

Another innovation of the present study was documenting precipitation, dynamical convergence, and advection for subregions of the main budget region corresponding to different combinations of dropsonde subsets. Large variability at spatial scales of $\sim 50 \text{ km}$ was present in all budget terms, and surface rain rate ranged from 0.5 to 9.8 mm h^{-1} , dynamical convergence of water vapor ranged from -1.5 to 11.3 mm h^{-1} , and advection of IWV ranged from -5.9 to 3.0 mm h^{-1} , among subregions.

Moreover, it was found that rain rate increased linearly with dynamical convergence across subregions, indicating a near-balance between convergence of moisture into a subregion and its removal by precipitation. Horizontal advection of IWV had no association with precipitation, as might be expected in the absence of orography. The substantial spatial heterogeneity in processes controlling IWV is smoothed out when averaging to larger budget regions.

A third innovation of the present study is an assessment of whether the water vapor budget of the main region could be observationally closed. One prerequisite for such a calculation is a measure of IWV tendency independent from the process terms. This was obtained by taking the difference between IWV measured by dropsonde around 1930 UTC and IWV reported by a satellite that passed over at 1615 UTC. A second prerequisite is robust estimation of uncertainty associated with measurement and sampling, which was also developed in the present study. Combining the dynamical convergence, precipitation, advection, and evaporation terms yielded an IWV tendency in the Eulerian reference frame equal to $-1.7 \pm 0.4 \text{ mm h}^{-1}$ for the main budget region. This was compared with an IWV tendency equal to $-0.5 \pm 0.6 \text{ mm h}^{-1}$ that was derived from the difference between dropsonde IWV and satellite IWV 3 h earlier. Excluding the advection term yielded an IWV tendency in the Lagrangian reference frame equal to $-0.3 \pm 0.4 \text{ mm h}^{-1}$. This was compared to an IWV tendency equal to $-1.2 \pm 0.8 \text{ mm h}^{-1}$ derived from the difference between dropsonde IWV and satellite IWV at the location where the budget region air column was 3 h earlier. As a result, the water vapor budget was nearly closed within the range of observational uncertainty for the Lagrangian reference frame and less so for the Eulerian reference frame. The most likely reason for lack of budget closure was that the IWV tendency derived from processes controlling IWV was representative of a time period less than an hour whereas the IWV tendency derived from the difference between dropsonde and satellite was an average over 3 h. When the uncertainty range was increased to include account for temporal representativeness, the water vapor budget became observationally closed.

While a single set of aircraft, shipboard, and satellite measurements for one area of an AR on one day is not sufficient to fully characterize physical processes governing the water budget in all areas of an AR and is not representative of all ARs, the method and preliminary results presented in this paper demonstrate that it is possible to observationally assess all major terms of the water vapor budget for a region in the core of an AR. The presence of large spatial and temporal heterogeneity suggests that uncertainty can be reduced by increasing the sampling density in space and time. This would better resolve dynamical convergence, precipitation, and advection occurring at $\sim 50\text{-km}$ spatial scales, and it would also obtain a better temporal match between IWV tendency calculated from physical process terms and IWV calculated by the difference in IWV measured at two different times. A better estimate of precipitation can be obtained with improved radar sampling, calibration, and conversion to surface rain rate, and the ability to independently measure precipitation and the IWV increase due to dynamical convergence will reduce the greatest sources of closure uncertainty in frontal sector IWV

tendency reported by the reanalysis study of Guan et al. (2020). Since Guan et al. report less uncertainty for the postfrontal, prefrontal, and pre-AR sectors of an AR, obtaining observational budget closure will be even more tractable for zones outside the AR core where precipitation is weaker and dynamic moistening or drying dominate.

Acknowledgments. This work was supported by the U.S. Army Corp of Engineers from the Award USACE W912HZ-15-2-0019 and the California Department of Water Resources Atmospheric River Program under Grant 4600010378 TO#15 Am 22. The contribution of authors Tanelli and Waliser was carried out on behalf of the Jet Propulsion Laboratory, California Institute of Technology, under a contract with NASA. SSMIS data are produced by Remote Sensing Systems and are sponsored by the NASA Earth Science ERRORS Project.

Data availability statement. SSMIS data are available at <http://www.remss.com>. NOAA aircraft dropsonde and radar data are available at <https://seb.noaa.gov/pub/acdata>, and R/V Ronald H. Brown data are available at <https://www.arm.gov/research/campaigns/amf2015apex>. MERRA-2 reanalysis data are available at <https://disc.gsfc.nasa.gov/>.

REFERENCES

- American Meteorological Society, 2019: Atmospheric river. *Glossary of Meteorology*, https://glossary.ametsoc.org/wiki/Atmospheric_river.
- Awaka, J., T. Iguchi, H. Kumagai, and K. Okamoto, 1997: Rain type classification for TRMM precipitation radar. *Proc. 1997 IEEE Int. Geoscience and Remote Sensing Symp.*, Singapore, IEEE, 1633–1635, <https://doi.org/10.1109/IGARSS.1997.608993>.
- Bao, J.-W., S. A. Michelson, P. J. Neiman, F. M. Ralph, and J. M. Wilczak, 2006: Interpretation of enhanced integrated water vapor bands associated with extratropical cyclones: Their formation and connection to tropical moisture. *Mon. Wea. Rev.*, **134**, 1063–1080, <https://doi.org/10.1175/MWR3123.1>.
- Bony, S., and B. Stevens, 2019: Measuring area-averaged vertical motions with dropsondes. *J. Atmos. Sci.*, **76**, 767–783, <https://doi.org/10.1175/JAS-D-18-0141.1>.
- Bretherton, C. S., M. Widmann, V. P. Dymnikov, J. M. Wallace, and I. Bladé, 1999: The effective number of spatial degrees of freedom of a time-varying field. *J. Climate*, **12**, 1990–2009, [https://doi.org/10.1175/1520-0442\(1999\)012<1990:TENOSD>2.0.CO;2](https://doi.org/10.1175/1520-0442(1999)012<1990:TENOSD>2.0.CO;2).
- Cordeira, J. M., F. M. Ralph, and B. J. Moore, 2013: The development and evolution of two atmospheric rivers in proximity to western North Pacific tropical cyclones in October 2010. *Mon. Wea. Rev.*, **141**, 4234–4255, <https://doi.org/10.1175/MWR-D-13-00019.1>.
- Fairall, C. W., E. F. Bradley, D. P. Rogers, J. B. Edson, and G. S. Young, 1996: Bulk parameterization of air-sea fluxes for Tropical Ocean-Global Atmosphere Coupled-Ocean Atmosphere Response Experiment. *J. Geophys. Res.*, **101**, 3747–3767, <https://doi.org/10.1029/95JC03205>.
- , —, J. E. Hare, A. A. Grachev, and J. B. Edson, 2003: Bulk parameterization of air-sea fluxes: Updates and verification for the COARE algorithm. *J. Climate*, **16**, 571–591, [https://doi.org/10.1175/1520-0442\(2003\)016<0571:BPOASF>2.0.CO;2](https://doi.org/10.1175/1520-0442(2003)016<0571:BPOASF>2.0.CO;2).
- Gelaro, R., and Coauthors, 2017: The Modern-Era Retrospective Analysis for Research and Applications, version 2 (MERRA-2). *J. Climate*, **30**, 5419–5454, <https://doi.org/10.1175/JCLI-D-16-0758.1>.

- Guan, B., and D. E. Waliser, 2015: Detection of atmospheric rivers: Evaluation and application of an algorithm for global studies. *J. Geophys. Res. Atmos.*, **120**, 12 514–12 535, <https://doi.org/10.1002/2015JD024257>.
- , —, and F. M. Ralph, 2020: A multi-model evaluation of the water vapor budget in atmospheric rivers. *Ann. N. Y. Acad. Sci.*, **1472**, 139–154, <https://doi.org/10.1111/nyas.14368>.
- Hilburn, K. A., and F. J. Wentz, 2008: Intercalibrated passive microwave rain products from the unified microwave ocean retrieval algorithm. *J. Appl. Meteor. Climatol.*, **47**, 778–794, <https://doi.org/10.1175/2007JAMC1635.1>.
- Hunter, S. M., 1996: WSR-88D radar rainfall estimation: Capabilities, limitations and potential improvements. *Natl. Wea. Dig.*, **20**, 26–38.
- Kunkee, D., G. A. Poe, D. Boucher, S. Swadley, Y. Hong, J. Wessel, and E. Uliana, 2008: Design and evaluation of the first Special Sensor Microwave Imager/Sounder (SSMIS). *IEEE Trans. Geosci. Remote Sens.*, **46**, 863–883, <https://doi.org/10.1109/TGRS.2008.917980>.
- Lavers, D. A., and G. Villarini, 2013: The nexus between atmospheric rivers and extreme precipitation across Europe. *Geophys. Res. Lett.*, **40**, 3259–3264, <https://doi.org/10.1002/grl.50636>.
- Löffler-Mang, M., and J. Joss, 2000: An optical disdrometer for measuring size and velocity of hydrometeors. *J. Atmos. Oceanic Technol.*, **17**, 130–139, [https://doi.org/10.1175/1520-0426\(2000\)017<0130:AODFMS>2.0.CO;2](https://doi.org/10.1175/1520-0426(2000)017<0130:AODFMS>2.0.CO;2).
- Marshall, J. S., and W. McK. Palmer, 1948: The distribution of raindrops with size. *J. Meteor.*, **5**, 165–166, [https://doi.org/10.1175/1520-0469\(1948\)005<0165:TDORWS>2.0.CO;2](https://doi.org/10.1175/1520-0469(1948)005<0165:TDORWS>2.0.CO;2).
- Martner, E. B., S. E. Yuter, A. B. White, S. Y. Matrosov, D. E. Kingsmill, and F. M. Ralph, 2008: Raindrop size distributions and rain characteristics in California coastal rainfall for periods without a radar bright band. *J. Hydrometeorol.*, **9**, 408–425, <https://doi.org/10.1175/2007JHM924.1>.
- McBride, J. L., B. W. Gunn, G. J. Holland, T. D. Keenan, and N. E. Davidson, 1989: Time series of total heating and moistening over the Gulf of Carpentaria radiosonde array during AMEX. *Mon. Wea. Rev.*, **117**, 2701–2713, [https://doi.org/10.1175/1520-0493\(1989\)117<2701:TSOTHA>2.0.CO;2](https://doi.org/10.1175/1520-0493(1989)117<2701:TSOTHA>2.0.CO;2).
- Meneghini, R., and T. Kozu, 1990: *Spaceborne Weather Radar*. Artech House, 199 pp.
- Neiman, P. J., L. J. Schick, F. M. Ralph, M. Hughes, and G. A. Wick, 2011: Flooding in western Washington: The connection to atmospheric rivers. *J. Hydrometeorol.*, **12**, 1337–1358, <https://doi.org/10.1175/2011JHM1358.1>.
- , G. A. Wick, B. J. Moore, F. M. Ralph, J. R. Spackman, and B. Ward, 2014: An airborne study of an atmospheric river over the subtropical Pacific during WISPAR: Dropsonde budget-box diagnostics, and precipitation impacts in Hawaii. *Mon. Wea. Rev.*, **142**, 3199–3223, <https://doi.org/10.1175/MWR-D-13-00383.1>.
- , B. J. Moore, A. B. White, G. A. Wick, J. Aikins, D. L. Jackson, J. R. Spackman, and F. M. Ralph, 2016: An airborne and ground-based study of a long-lived and intense atmospheric river with mesoscale frontal waves impacting California during CalWater-2014. *Mon. Wea. Rev.*, **144**, 1115–1144, <https://doi.org/10.1175/MWR-D-15-0319.1>.
- , and Coauthors, 2017: An analysis of coordinated observations from NOAA's Ronald H. Brown Ship and G-IV aircraft in a landfalling atmospheric river over the North Pacific during CalWater-2015. *Mon. Wea. Rev.*, **145**, 3647–3669, <https://doi.org/10.1175/MWR-D-17-0055.1>.
- Paltan, H., D. Waliser, W. H. Lim, B. Guan, D. Yamazaki, R. Pant, and S. Dadson, 2017: Global floods and water availability driven by atmospheric rivers. *Geophys. Res. Lett.*, **44**, 10 387–10 395, <https://doi.org/10.1002/2017GL074882>.
- Peng, G., H.-M. Zhang, H. P. Frank, J.-R. Bidlot, M. Higaki, S. Stevens, and W. R. Hankins, 2013: Evaluation of various surface wind products with OceanSITES buoy measurements. *Wea. Forecasting*, **28**, 1281–1303, <https://doi.org/10.1175/WAF-D-12-00086.1>.
- Ralph, F. M., P. J. Neiman, and G. A. Wick, 2004: Satellite and CALJET aircraft observations of atmospheric rivers over the eastern North Pacific Ocean during the winter of 1997/98. *Mon. Wea. Rev.*, **132**, 1721–1745, [https://doi.org/10.1175/1520-0493\(2004\)132<1721:SACAOO>2.0.CO;2](https://doi.org/10.1175/1520-0493(2004)132<1721:SACAOO>2.0.CO;2).
- , —, and R. Rotunno, 2005: Dropsonde observations in low-level jets over the northeastern Pacific Ocean from CALJET-1998 and PACJET-2001: Mean vertical-profile and atmospheric-river characteristics. *Mon. Wea. Rev.*, **133**, 889–910, <https://doi.org/10.1175/MWR2896.1>.
- , —, G. A. Wick, S. I. Gutman, M. D. Dettinger, D. R. Cayan, and A. B. White, 2006: Flooding on California's Russian River: Role of atmospheric rivers. *Geophys. Res. Lett.*, **33**, L13801, <https://doi.org/10.1029/2006GL026689>.
- , and Coauthors, 2016: CalWater field studies designed to quantify the roles of atmospheric rivers and aerosols in modulating U.S. West coast precipitation in a changing climate. *Bull. Amer. Meteor. Soc.*, **97**, 1209–1228, <https://doi.org/10.1175/BAMS-D-14-00043.1>.
- , and Coauthors, 2017: Dropsonde observations of total integrated water vapor transport within North Pacific atmospheric rivers. *J. Hydrometeorol.*, **18**, 2577–2596, <https://doi.org/10.1175/JHM-D-17-0036.1>.
- , J. J. Rutz, J. M. Cordeira, M. Dettinger, M. Anderson, D. Reynolds, L. J. Schick, and C. Smallcomb, 2019: A scale to characterize the strength and impacts of atmospheric rivers. *Bull. Amer. Meteor. Soc.*, **100**, 269–289, <https://doi.org/10.1175/BAMS-D-18-0023.1>.
- Seager, R., and N. Henderson, 2013: Diagnostic computation of moisture budgets in the ERA-Interim reanalysis with reference to analysis of CMIP-archived atmospheric model data. *J. Climate*, **26**, 7876–7901, <https://doi.org/10.1175/JCLI-D-13-00018.1>.
- Viale, M., R. Valenzuela, R. D. Garreaud, and F. M. Ralph, 2018: Impacts of atmospheric rivers on precipitation in southern South America. *J. Hydrometeorol.*, **19**, 1671–1687, <https://doi.org/10.1175/JHM-D-18-0006.1>.
- Wentz, F. J., 1995: The intercomparison of 53 SSM/I water vapor algorithms. Remote Sensing Systems Tech. Rep. on WetNet Water Vapor Intercomparison Project (VIP), 19 pp.
- Wimmers, A. J., and C. S. Velden, 2011: Seamless advective blending of total precipitable water retrievals from polar-orbiting satellites. *J. Appl. Meteor. Climatol.*, **50**, 1024–1036, <https://doi.org/10.1175/2010JAMC2589.1>.
- Winters, A. C., and J. E. Martin, 2017: Diagnosis of a North American polar-subtropical jet superposition employing piecewise potential vorticity inversion. *Mon. Wea. Rev.*, **145**, 1853–1873, <https://doi.org/10.1175/MWR-D-16-0262.1>.
- Wong, S., A. D. Del Genio, T. Wang, B. Kahn, E. J. Fetzer, and T. S. L'Ecuyer, 2016: Responses of tropical ocean clouds and precipitation to the large-scale circulation: Atmospheric water budget-related phase space and dynamical regimes. *J. Climate*, **29**, 7127–7143, <https://doi.org/10.1175/JCLI-D-15-0712.1>.
- Zhu, Y., and R. E. Newell, 1998: A proposed algorithm for moisture fluxes from atmospheric rivers. *Mon. Wea. Rev.*, **126**, 725–735, [https://doi.org/10.1175/1520-0493\(1998\)126<0725:APAFMF>2.0.CO;2](https://doi.org/10.1175/1520-0493(1998)126<0725:APAFMF>2.0.CO;2).